DEVELOPMENT OF A NANOCOMPOSITE SENSOR AND ELECTRONIC SYSTEM FOR MONITORING OF LOCOMOTION OF A SOFT EARTHWORM ROBOT

A Dissertation
Presented to
The Academic Faculty

by

Riccardo Goldoni

In Partial Fulfillment
of the Requirements for the Degree
Master of Science in the
School of Materials Science and Engineering

Georgia Institute of Technology
August 2020

DEVELOPMENT OF A NANOCOMPOSITE SENSOR AND ELECTRONIC SYSTEM FOR MONITORING OF LOCOMOTION OF A SOFT EARTHWORM ROBOT

Approved by:

Dr. Woonhong Yeo, Advisor
School of Mechanical Engineering
Georgia Institute of Technology

Dr. Seung Soon Jang
School of Materials Science and Engineering
Georgia Institute of Technology

Dr. Sundaresan Jayaraman
School of Materials Science and Engineering
Georgia Institute of Technology

Date Approved: April 10, 2020

To my grandmother Laura and my dear friend Nicolò, who aren't able to enjoy this day with me but will be surely watching

"Sicuramente i più coraggiosi sono coloro che hanno la visione più chiara di ciò che li aspetta, così della gloria come del pericolo, e tuttavia l'affrontano"

ACKNOWLEDGEMENTS

I would like to especially thank my mother Alessandra and my father Massimo without whose continuous support I would not be here. I would also like to thank my brother Filippo for being present both in joy and sadness, always pushing me to strive for greatness. I extend my gratitude to my relatives, who always made me feel appreciated for what I was doing here, no matter the outcomes.

Finally, I would like to thank my research advisor and my lab mates whose experience and advice made me grow both personally and professionally as a researcher.

TABLE OF CONTENTS

LIST OF TABLES

LIST OF FIGURES

LIST OF SYMBOLS AND ABBREVIATIONS

CNT	=	Carbon nanotubes
SWCNT	=	Single-walled carbon nanotubes
MWCNT	=	Multi-walled carbon nanotubes
PDMS	=	Polydimethylsiloxane
NW	=	Nanowire
CB	=	Carbon black
NP	=	Nanoparticles
GF	=	Gauge factor
PCB	=	Portable circuit board
ACF	=	Anisotropic conductive film
PVA	=	Polyvinyl alcohol

SUMMARY

The ability to detect external stimuli and perceive the surrounding areas represents a key feature of modern soft robotic systems, used for exploration of harsh environments. Although people have developed various types of biomimetic soft robots, no integrated-sensor system is available to provide feedback locomotion. Here, a stretchable nanocomposite strain sensor with integrated wireless electronics to provide a feedback-loop locomotion of a soft robotic earthworm is presented. The ultrathin and soft strain sensor based on a carbon nanomaterial and a low-modulus silicone elastomer allows for a seamless integration with the body of the soft robot, accommodating large strains derived from bending, stretching, and physical interactions with obstacles. A scalable, cost-effective, screen-printing method manufactures an array of strain sensors that are conductive and stretchable over 100% with a gauge factor over 38. An array of stretchable nanomembrane interconnectors enables a reliable connection between soft strain sensors and wireless electronics, while tolerating the robot's multi-modal movements. A set of computational and experimental studies of soft materials, stretchable mechanics, and hybrid packaging provides key design factors for a reliable, nanocomposite sensor system. The miniaturized wireless circuit, embedded in the robot joint, offers a real-time monitoring of strain changes on the earthworm skin. Collectively, the soft sensor system shows a great potential to be integrated with other flexible, stretchable electronics for applications in soft robotics, wearable devices, and human-machine interfaces.

CHAPTER 1. INTRODUCTION

The field of robotics has seen an increasing interest among the scientific community due to combined advances in the field of materials science, physics and electronics that are now able to give these robots unprecedented capabilities. Robots are not only able to complete duties more precisely and at a faster pace, but they are also becoming capable of performing tasks that humans can't accomplish. Based on the domain of operation, manufacturers decide to give these robots specific properties. Those that should repeat commands precisely at a high speed usually possess rigid components for reliability and necessary strength. Conversely, a more recent field branch of this field, soft robotics, focuses on the realization of complex robotic systems inspired from the biological world. In fact, both humans and animals possess an overall soft body where the rigid component is only limited to the skeleton [1].

Studying animals performing their daily tasks provided the necessary foundation to biomimetic manufacturing of robots. Many examples can be found in literature of robots capable of swimming [2-4], rolling [5, 6] jumping [7-10], grasping [11-13], crawling [11, 14] and performing basic locomotion [15-22]. A wide variety of animals, such as jellyfishes [4], fishes [2], octopuses [11], frogs [10], salamanders [22], snakes [23], rabbits [24], insects [9], caterpillars [14, 16] and earthworms [18, 20, 21, 25, 26] has inspired the design and fabrication of bio-inspired robots. Among these, the study of earthworms' locomotion has attracted great interest due to potential applications in environmental exploration [27].

The fundamental principle at the basis of locomotion of every animal is the ability to perceive both the encumbrance of its body (proprioception) and the external environment (exteroception) [28]. Rigid robots made of non-deformable materials are facilitated in proprioception because their movements are regulated by mechanical joints with limited degrees of freedom. Conversely, this becomes more challenging for soft robots that have deformable bodies and consequently possess a substantially higher number, almost infinite, of degrees of freedom. In order to make robots capable of such perception, they need to be equipped with sensors that can emulate physical sensations felt by humans and animals. Many sensing technologies are employed when fabricating such sensors: the most commonly employed are resistive [29-32] and piezoresistive sensors [33-36], capacitive sensors [37, 38] and optical sensors [39-41]. There are also plenty of choices in the nature of the sensing component that can be a liquid metal [29], a conductive nanocomposite [33-35, 37, 42], a nanomaterial (AgNWs [43], CNTs [29] and graphene [44]), a ionic liquid [30, 31], an optical fiber [40, 41] or conductive yarn/fabric [32, 36, 38]. These sensors must fulfill requirements of elasticity and durability to be suitable for integration on the body of a soft robot. For such reason most of the strain and tactile sensors are realized on either elastomeric (i.e. Ecoflex, Dragonskin, PDMS) or rubber substrates. Many sensors have been developed that are capable of quantifying stress, strain and pressure, however being able to integrate all these functions at the same time still remains a challenge for many research groups [45].

This study reports the design and development of a highly stretchable nanocomposite strain sensor with dedicated electronic system, integrated on the body of soft robotic earthworm, for feedback-loop locomotion. The robot acquires proprioception and

exteroception abilities thanks to the high sensitivity of the strain sensor (GF > 38), that is therefore used to sense the surrounding environment and guide its locomotion. The overall system is robust and compliant with the robot movements, as both the strain sensor and the stretchable connectors employed for data transfer are embedded in an outer layer of silicone. The portable circuit board (PCB) that enables collection, processing and real time wireless transfer of data, is allocated in a customized 3D-printed case inside the rigid segments of the worm, therefore isolated from any type of external stress. The excellent performance of the sensor in terms of stretchability, sensitivity and consistency over time, makes it an interesting candidate for applications in robotics, especially for environmental exploration.

1.1 Object of the Study

The goal of this study is to realize a strain sensor and electronic system to monitor the locomotion of a soft robotic earthworm. The fabrication of the sensor by a low-cost high-throughput technique is followed by the assembly of a dedicated printed circuit board (PCB) and seamless integration of the system on the robot body. The specific objectives of the study are listed below:

- Fabricate a highly sensitive strain sensor able to accommodate large strains, up to 100%, without loss in performance
- Propose a method to fabricate such sensors with a high throughput low-cost technique, maintaining consistency in the fabrication outcome between different sensors

- Demonstrate the integration of the sensor on the robotic system and the successful achievement of its function to monitor the robot locomotion wirelessly.

1.2 Thesis Outline

Chapter 2 presents preliminary information regarding the conductive material employed to give the sensing capability to the sensor, carbon nanotubes. An explanation of the strain sensing mechanism is provided, along with an overview of different applications of these sensors. Moreover, performance parameters are introduced, that are fundamental when comparing different strain sensors and assess their suitability for a specific application. The last part of Chapter 2 is used to explain the concept of fractal designs and, particularly, of Peano curves, geometrical patterns employed in the fabrication of the sensors and key factor in achieving high stretchability of the device.

In Chapter 3, the materials used in the study are presented, with a focus on both the conductive component and the substrate, whose combination guarantees to have a highly sensitive and highly stretchable device. The characterization techniques employed in the study are also reported. One part of Chapter 3 is dedicated to the fabrication method, that is explained in detail and compared to other fabrication techniques providing fundamental reasoning to choose such technique instead of others available.

In the first part of Chapter 4, the design and fabrication of the strain sensor are reported. Starting from the motivation explained in Chapter 2 to use space-filling curves, a thorough explanation of how the geometry of the pattern determine the ultimate stretchability of the conductive trace is provided, that is a key factor of this study. The last part of Chapter 4 focuses instead on the printed circuit board design and the integration of

the sensor with such board. Explanations are provided, where required, for the use of some components in assembling the circuit and a particular attention is reserved to the stretchable connectors used to link the sensor and the PCB, being that one of the challenges encountered in the study.

Chapter 5 addresses the integration of our electronic system on the soft robotic earthworm whose locomotion is subject of the study. The positioning of the sensors on the segments of the robot is explained and reasoning for these choices is provided. An overview of the locomotion mechanism is presented and ultimately the results of the successful monitoring of this locomotion using a mobile device are provided.

Lastly, Chapter 6 is used for discussion and summary of the experimental findings relative to the study. Possible use cases for such technology are addressed along with insights on future work that could improve the system described in this thesis.

CHAPTER 2. LITERATURE REVIEW

2.1 Carbon Nanotubes

Carbon allotropes manifests substantially different properties depending on how the atoms of carbon are bonded together. Graphite and diamond are without any doubt the most renowned among them [46]. However, the serendipitous discovery made by Kroto *et al.* [47] in 1985 of a stable structure consisting of a cluster of 60 atoms of carbon, renamed Buckminsterfullerene, arose an increasing interest regarding the synthesis of newer carbon allotropes. As a result of this effort, new structures were discovered following the Buckminsterfullerene. Iijima in 1991 [47] first reported the discovery of carbon nanotubes, while later in 2004 it was the turn of Novoselov *et al.*, that described the discovery of few atoms thick graphitic layers that acquired the name of graphene [48].

Carbon nanotubes can practically be seen as elongated fullerenes, creating a cylindrical structure where the length is notably greater than the diameter, conferring peculiar properties to this structure. The body of the fullerene is made of a sheet of graphene that is rolled forming an open tube. This tube is then closed at its ends by two pieces of fullerenes completing the cylindrical structure proper of carbon nanotubes [49].

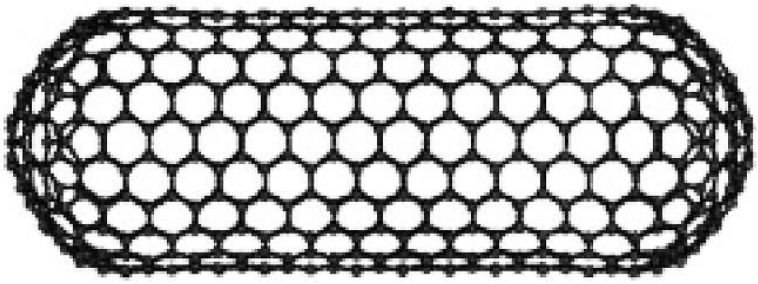

Figure 1 Tubular structure of a carbon nanotube [49]

Carbon nanotubes possess another peculiar geometrical property: helicity. The way the graphene sheet gets folded to form an open nanotube determines the helical structure. This discovery was revealing as the helical parameters and the diameter of the tube were found to be determinant for the final properties of the nanotubes. A graphene sheet can be rolled up into a cylinder only if the conditions deriving from the Bravais lattice vectors are satisfied.

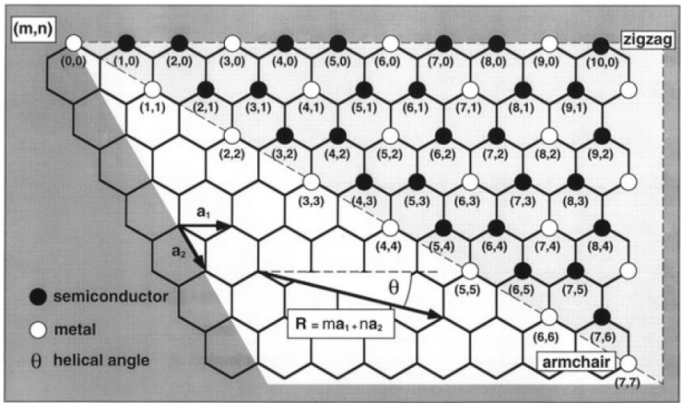

Figure 2 Indexing scheme of a planar graphene sheet [49]

Figure 2 shows the indexing scheme that determines the helicity of the carbon nanotube after the folding process. Depending on the folding direction a carbon nanotube can be classified as:

- Armchair: nanotube axis normal to the 30° direction

- Zigzag: nanotube axis normal to the 0° direction
- Chiral: nanotube axis normal to a direction with angle comprised between 0 and 30°

A schematic model of an armchair (a), zigzag (b) and chiral (c) nanotube is reported in Figure 3 below.

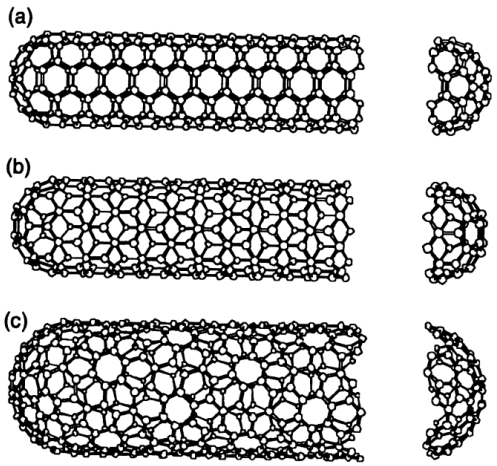

Figure 3 Graphical representation of carbon nanotubes with different helical parameters [50]

Apart from the intrinsic geometry of a single carbon nanotube, nanotubes exist in three main varieties depending on the number of walls they possess. Multiwalled carbon nanotubes consist of concentric carbon nanotubes each one spaced by a distance that is slightly larger compared to that of graphene sheets (0.335 nm), due to geometric constraints [51]. Double-walled carbon nanotubes are a type of coaxial nanostructure where two carbon nanotubes are nested. Even if they belong to the family of multiwalled carbon nanotubes, they are normally considered as a category themselves due to their unique properties. Finally, single-walled carbon nanotubes are the most simple and pristine structure of this kind of materials.

2.1.1 Mechanical Properties

Carbon nanotubes possess mechanical properties that make them particularly interesting for many applications. The intrinsic strength of these nanostructures derives in first place from the C-C planar covalent bond, among the strongest in nature. It is important, however, to differentiate between the properties of a single-walled carbon nanotube (SWCNT) and a multi-walled carbon nanotube (MWCNT), as in many cases they do not coincide precisely. Such slight differences could play a major role in applications where high accuracy is required and attention is given to minimum details, reason for the importance of this differentiation. Many studies have investigated the matter either by theoretical predictions or experimental measurements, or a combination of both [52]. Yu *et al.* investigated the response of both SWCNT [53] and MWCNT [54] to a tensile test, reporting differences between the two, as anticipated. SWCNT were found to have a Young modulus ranging from 320 to 1470 GPa while MWCNT showed notably lower values, from 270 to 950 GPa. The stress-strain curves for both SWCNT and MWCNT are reported in Figure 4.

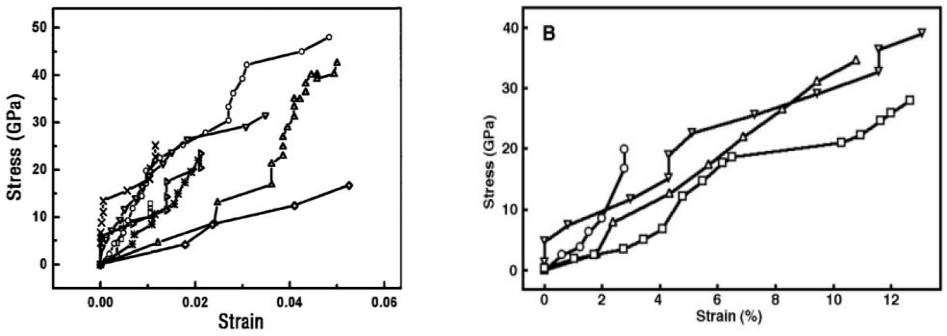

Figure 4 Stress-strain curves for SWCNT (left) and MWCNT (right) under tensile load [54]

Although exceptional in terms of tensile strength their behavior is far from being optimal when they undergo compression. Having a length *l* considerably greater than their diameter *d* makes them a high-aspect ratio material. This high-aspect ratio and the peculiar hollow structure provide reasoning for such a poor performance in compression. In fact, when subjected to compression, torsion or bending they undergo buckling, resulting in deformations in the atomic structure of the nanotube that are not recoverable. Values of the Young's modulus for both SWCNT and MWCNT have been obtained by means of Raman spectroscopy in previous studies. Lourie and Wagner [55] reported values of 2.8-3.6 TPa for SWCNT and 1.7-2.4 TPa for MWCNT showing an incredible resistance to being deformed elastically. The difference between the values obtained for SWCNT and MWCNT can be attributed to the interaction between nested nanotubes, creating shear stress on their surface, consequently reducing the overall strength.

2.1.2 Electrical Properties

Motivated by an increasing interest for the use of carbon nanotubes for electronic applications, many studies have focused on investigating the intrinsic electrical properties of a single nanotube. A study conducted by Thio *et al.* first reported how both the helicity of the structure and the diameter of the tubule were responsible for the metallic or semiconducting nature of the nanotube. However, due to the challenges encountered in experimental measurements, it was only possible to report how in a bundle of nanotubes usually a fraction of those are metallic and another part are semiconducting [56].

While the differences in mechanical behavior of CNTs can be attributed to their variants (MWCNT or SWCNT), the electrical properties are mainly directly determined by

their structure: armchair, zigzag and chiral all conduct electricity differently [50]. Specifically, in order to be considered conductive the structure of a carbon nanotubes must fulfil Equation 1:

$$2n + m = 3q \tag{1}$$

where q must be an integer. Armchair configurations always satisfy this condition and thus have a metallic behavior, while zigzag and chiral can be either metallic or semiconductors (Figure 5).

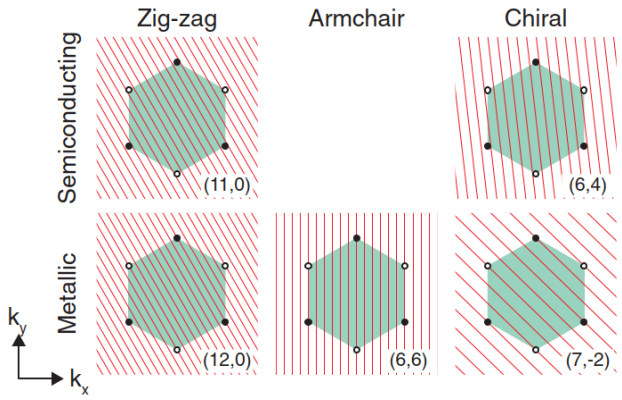

Figure 5 Quantization lines for each helical configuration [57]

The degree of conductivity of these nanotubes derives from their geometrical dimensions as well, as the semiconducting band gap has been proven to be proportional to the reciprocal of the diameter *1/d* [58].

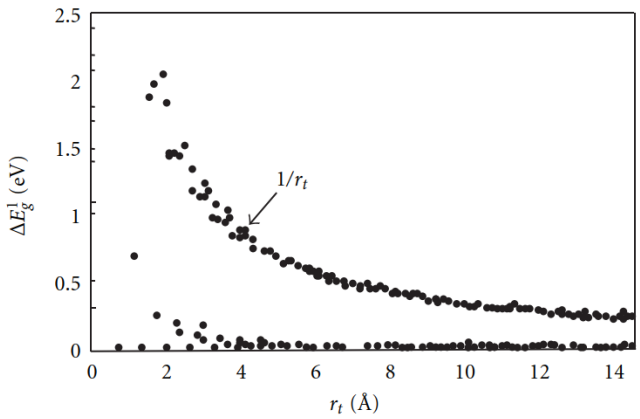

Figure 6 Primary band gap behavior with increasing nanotube radius [58]

Interesting is that nanotubes possessing different degree of conductivity are stable when paired together. As a result, it was possible to realize an electronic shielded wire created by concentric nanotubes with the inner cylinder being metallic and the outer being semiconductor (insulating) [59].

2.1.3 Electromechanical Properties

The almost infinite possibilities enabled by the combination of different tubule diameters and helical structures gave birth to a wide range of available gap sizes, allowing to control the semiconducting properties of carbon nanotubes. As a result, many research groups have investigated into the electromechanical properties of these nanostructures. Tension, torsion and bending have been applied to CNTs possessing different chirality [54, 60-63]. Other groups have simulated these interactions using either tight binding (TB) methods or density functional theory (DFT) [64].

The conductivity of metallic CNTs is hindered by strain at the point of reaching a value near zero before fracture. On the other hand, the semiconducting behavior is maintained independently of the strain applied [65]. A change in band gap, resulting from an applied

strain, lead to a change in the electrical resistance of the carbon nanotube. This peculiar behavior of CNTs have made them a promising candidate for the fabrication of nanocomposite strain sensors.

2.2 Strain Sensors

Strain sensors are those devices used to measure deformations or sense pressure. They respond to mechanical deformations with a variation of resistance or capacitance, which produces an electrical signal as output. By analysis of this electrical signal, it is possible to quantify the amount of strain the sensor has undergone or estimate the applied pressure.

The nature of strain sensors changes deeply, as their application is substantially different. Piezoceramic (PZT) and piezofilm (PVDF) sensors, for instance, are mainly employed in smart structural systems and they leverage the intrinsic piezoelectric nature of some materials to function as sensors [66]. Fiber Bragg grating sensors are used in optical systems and they detect small wavelength shifts associated with strain and quantify these deformations. However, they require sophisticated equipment to be able to accurately detect these small spectral displacements, reason for which their application is limited [67, 68]. Raman strain rosettes exploits the Raman properties of some nanomaterials (e.g. CNTs) to measure micro-strains. These sensors are limited in terms of the extent of measurable strain, and, as it is the case for Fiber Bragg grating sensors, they require sophisticated equipment [69].

Although many other types of strain sensors exist, tailored for specific applications, the most common ones are resistive-type and capacitive-type strain sensors. Their widespread adoption arises from the simplicity of the detecting system., the ease of

fabrication and an overall good dynamic performance. Moreover, these sensors are extremely flexible in terms of their application. Resistive-type sensors are based on flexible (or stretchable, depending or the requirements) substrates, where a conductive trace change its resistance when undergoing deformation. As it will be explained in more detail after, many are the causes underlying this change in resistance. Capacitive-type sensors, on the other hand, are based on a triple-layered structure where two electrodes are placed on opposite sides of a dielectric layer. As a result of tensile strain, these two electrodes come closer, causing a change in the capacitance of the sensor.

2.2.1 Fabrication Techniques

Strain sensors work in different ways depending on the fabrication process and the type of conductive material employed as sensing component. Recent advancements made in printing technologies created a plethora of different opportunities to realize such sensor. Research groups have fabricated strain sensor using screen printing [70], inkjet printing [71], aerosol jet printing [72], 3D-printing [73], coaxial printing [74], electrohydrodynamic (EHD) printing [75] and transfer printing [76].

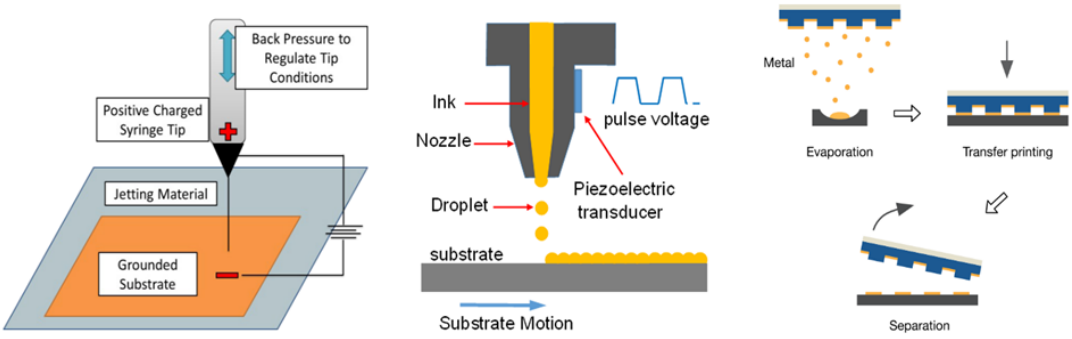

Figure 7 EHD (left) [75], inkjet (middle) [77] and transfer printing (right) [78] techniques

However, this list does not aim to be comprehensive as customized printing techniques are always permitted, allowing potentially unlimited choices of fabrication methods. Another fabrication technique that has been widely used to realize strain sensors is spray coating [79, 80] due to its low-cost and compatibility with many inks.

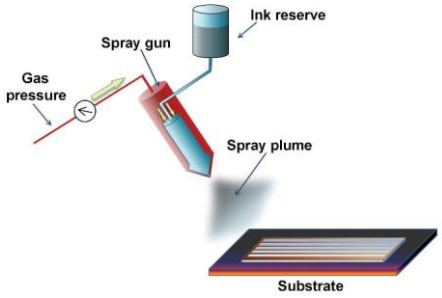

Figure 8 Spray coating process [81]

Other methods include filtration [82, 83] chemical synthesis [84] and chemical vapor deposition [85].

2.2.2 Strain Sensing Mechanism

Traditional strain gauges rely primarily on geometrical and piezoelectric effects to display their strain sensing capabilities. In the strain sensing behavior of nanocomposite devices, instead, many more factors are involved, such as disconnection, crack propagation and tunneling effect. Some of these are characteristic of specific nanomaterials while other can be considered as more general. For instance, the tunneling effect has proved to be the most relevant effect in the strain sensing mechanism of carbon nanotubes-polymer composites [58, 86-89].

As discussed before, strain sensors deeply differ in form, materials, sensing mechanism and application. Hereafter an exploration on resistive-type and capacitive-type

nanocomposite strain sensors is offered. However, the general principles of the strain sensing mechanism, geometrical and piezoresistive effect, also apply on other type of sensors. This mechanism follows two different rules depending on the nature of the sensor, resistive or capacitive.

For resistive sensors, an elongation on the x-direction causes a transverse strain perpendicular to the direction of the tensile stress. This behavior is regulated by the Poisson ratio ν, an intrinsic property of the material. Isotropic linear elastic materials possess a value of ν between -1.0 and 0.5 [90]. As a result, depending on the specific Poisson ratio of the substrate, dominating the mechanical deformation of the strain sensor, the length l and cross-sectional area A increases or decreases. The resistance of a conductor can be calculated using Equation 2:

$$R = \frac{\rho l}{A} \tag{2}$$

where ρ is the electrical resistivity. It is then evident how the resistance of the device increases with increasing length and decreasing cross-section.

Capacitive-type sensors comprises a dielectric layer sandwiched between two electrodes (or plates). A capacitor with two parallel electrodes with dimensions l (length) and w (width) at a distance d is taken as reference. The distance between the plates corresponds to the thickness of the dielectric layer. The constants ε_0 and ε_r represent the values of permittivity of the vacuum and the dielectric layer, respectively. It is possible to

show how the thickness of the layer determines the value of the capacitance *C* using Equation 3:

$$C = \varepsilon_0 \varepsilon_r \frac{wl}{d} \tag{3}$$

In fact, as the sensor undergoes tensile stress, the thickness of the dielectric layer decreases, leading to an increase of the value of capacitance *C*. Moreover, if we consider the Poisson's ratio of the electrodes and the dielectric layer to be equal, that is justified by the minor effect of the conductive material in nanocomposite sensors, it is possible to relate the change in capacitance directly to the applied strain, following Equation 4:

$$C = (1 + \varepsilon)C_0 \tag{4}$$

However, this relation holds true only for a limited amount of strain, after which the linear relation between axial and transverse strain is lost [91].

Piezoelectric materials produce an electrical signal when undergoing deformation. In a similar fashion, piezoresistive materials change their intrinsic resistance once stretched. In this case the equation controlling the piezoresistive effect is Equation 5:

$$\frac{\Delta R}{R} = (1 + 2\nu)\varepsilon + \frac{\Delta \rho}{\rho} \tag{5}$$

where the first term can be attributed to geometrical effects while the second represents the change the intrinsic piezoresistivity of the material. Piezoresistivity in nanocomposite

strain sensors however has been largely reported as contributing only marginally to the strain sensing mechanism of these devices as the nanomaterials frequently have a weak bonding to the polymer matrix [58, 92, 93].

The main reason for the substantial changes in the electrical resistance of a strain sensing device must be attributed to the continuity of the conductive pathway. Cracks or, more generally, disconnection points in this conductive pathway lead to a dramatic increase in the resistance. As stressed before, there are some mechanisms in nanomaterial-based strain sensors that are critical factors in determining the conductivity of this pathway.

To identify which mechanisms are more relevant than others, it is important to specify the nature of stretchable strain sensors based on flexible conductive polymer composites. This category of devices can be divided into three subcategories:

- Filled-type
- Sandwich-type
- Adsorption-type

Filled-type nanocomposites see a dispersion of conductive materials into a stretchable polymer matrix. Major requirement in the fabrication of such devices is a high loading of these conductive nanomaterials. This is due to the necessity to form a conductive pathway that gives the sensing ability to the device. This electrical conductivity is highly dependent on the concentration of conductive material. Specifically, there is a value called percolation threshold which needs to be reached in order to form the conductive pathway [94]. Huang proposed a relation that could be used to estimate such value [95] that is reported hereafter in Equation 6:

$$\sigma \propto (\chi - \chi_c)^t \quad (6)$$

where σ is the electrical conductivity, t is a critical exponent related to the conductive network dimensions, χ is the mass fraction of conductive material and χ_c is the percolation threshold.

As the fabrication cost of strain sensors highly depends on this threshold, many research groups have tried to lower this value. Costa *et al.* [96] for example, employed the use of surfactants to enhance the dispersion of CNTs, as their conductivity is mostly limited by the formation of CNT bundles, or agglomerates. Other groups tried to mix nanomaterials with different dimensions in order to exploit the complementarity of their structures (CNT/carbon black [97] and CNT/graphene [98]), achieving successful results when embedding them into a PDMS polymer matrix. Surface modification of conductive nanomaterials could also increase the electrical conductivity of the pathway improving their dispersion in the polymer matrix. However, in some cases, these modifications could also degrade the intrinsic conductivity of the nanomaterials.

Sandwich-type nanocomposites consist of a conductive layer trapped between two layers of polymer matrix. These sensors possess a shortcoming compared to the filled-type nanocomposites, as it is difficult to control the deposition of the conductive layer, in terms of homogeneity and density. In turn, they possess a higher sensitivity and lower hysteresis.

Lastly, adsorption-type nanocomposites rely on transfer or deposition of a layer of conductive material, which creates a coating stacked on top of the polymer substrate. In this case a good adhesion between these layers is essential for the stability of the sensor

after repeated stretching cycles. Surface modification of the polymer layer usually facilitate this adhesion. Silane coupling agents (SCA) are widely employed to modify the surface as they improve adhesion or dispersion of the conductive materials. As in the case of sandwich-type nanocomposites, the difficulty of the fabrication process relies on the precise control of the deposition of the conductive component, which is critical to ensure reproducibility and stability of the sensor.

In contrast with traditional strain gauges, where geometrical and piezoresistive effects are dominating, in nanocomposite strain sensors other factors have a bigger impact on the sensing behavior, specifically disconnection mechanism, crack propagation and tunneling effect. When a percolation network is formed, creating a conductive pathway in the sensor, electrons can flow along this path when nanomaterials overlap. However, when the sensor is stretched these nanomaterials slide away from each other reducing the conductivity of such path. As a result of this increased distance between materials and reduced overlapping, the resistivity of the device increases. This disconnection mechanism is further worsened when there is a weak adhesion between the conductive material and the polymer matrix.

Crack propagation can be considered an influential mechanism in sandwich-type and adsorption-type strain sensors mainly, as the filled-type composite sensors does not have a coated, deposited, or transferred conductive trace where cracks can propagate, but rather a nanomaterial dispersion. The conductive trace accumulate stress in certain points when getting stretched. When a certain stress limit is reached, microcracks start appearing, increasing the resistance of the trace to the point where a separation line gets defined, and the increase is resistance is significantly higher. Once the stress is released and the sensor regains its original shape, the two ends of the conductive trace come back in close contact

and the resistance decreases. However, the onset of multiple of these cracks produces a change of the initial resistance as the conductivity of the trace is irreversibly compromised. As the distance between the edges increase, so does the electrical resistance.

In some cases, having a prestrained substrate could help lowering the effect of these microcracks. Prestrained substrates normally present minimal out-of-plane buckling of the conductive traces that are then flattened once the device gets stretched. In doing so, they can accommodate a bigger strain without generating microcracks in the trace [99].

Even if nanomaterials are not in contact, however, electrons can still flow along the conductive path by crossing non-conductive barriers, thanks to the tunneling effect. This effect has proved to be playing a major role in determining the strain sensing behavior of CNTs-polymer nanocomposites [58, 87, 89]. In all the aforementioned kinds of nanocomposite sensors (filled-type, sandwich-type and adsorption-type) carbon nanotubes are dispersed in a polymer matrix and thin dielectric layers covering nanotubes can be observed at CNT-CNT junctions [86].

Simmons [100] in 1963 proposed a model to estimate the total resistance when quantum tunneling effects play a major role in the system. The resistance R is given by Equation 7:

$$R = \frac{V}{AJ} = \frac{h^2 d}{Ae^2\sqrt{2m\lambda}} \exp\left(\frac{4\pi d}{h}\sqrt{2m\lambda}\right) \tag{7}$$

where V is the potential difference, A is the area of the cross section of the tunneling junction, J is the current density at the tunneling junction, h is Plank's constant, d is the

distance between the nanomaterials, e and m are the charge and mass of an electron, respectively, and λ is the height of the energy barrier for the dielectric polymer material. Many studies have reported adherence of experimental data to the proposed model by Simmons [58, 87, 101].

Some of these parameters are affected by other factors such as the dispersion and morphology of the nanomaterials and the interaction between the nanomaterials and the polymer matrix. As an example, silver nanowires (AgNWs) and CNTs behave differently when the substrate is stretched. While AgNWs present the usual sliding mechanism leading to the disconnection phenomena, CNTs, that are mostly entangled in bundles, unfold into simpler structures causing a change in the tunneling resistance [91].

2.2.3 Performance Parameters

Many factors concurrently influence the behavior of strain sensors, as it has been presented above and, as a result, performance parameters are needed to ensure uniformity in evaluating the effectiveness of a certain device in its application. Depending on the application, some of these parameters are more important than others but it is also possible to appreciate how some of these are correlated.

2.2.3.1 Stretchability

The stretchability of a strain sensor represents the percentage of elongation the sensor can withstand before starting to tear apart, losing its structural integrity. Stretchability of a device can be tuned primarily deciding the type of substrate to employ. Given the frequent application of these device in healthcare or patient monitoring, the substrate is often chosen

to be biocompatible. Among these, silicone formulations such as Ecoflex, have arisen a certain interest, thanks to their exceptional stretchability and biocompatibility when in contact with the skin. Stretchability of the substrate, however, is not the only parameter that has to be taken into consideration when evaluating the stretchability of the device as a whole, as electrical conductivity must be guaranteed as well. A certain elongation could be withstanded by the substrate but not by the conductive trace, whose fracture would impair the functionality of the sensor. As a result, the fabrication technique plays an important role as much as the substrate do. Filled-type strain sensors are normally more stretchable than the sandwich-type or adsorption-type, given that in the last two cases the conductive trace is transferred, printed or deposited on the substrate, creating a greater mismatch between the two.

The morphology of the nanomaterial is another influent factor contributing to the final stretchability. 0D, 1D and 2D materials all behave differently when integrated into a more complex system. It is evident from literature how strain sensors based on 1D materials having high aspect ratio (AgNWs, CNTs, etc.), are notably more stretchable than strain sensors based on carbon black (CB), nanoparticles (NP) or graphene [85, 102-104].

2.2.3.2 Sensitivity

The sensitivity parameter is defined as the ratio between the change in electrical output produced by the strain sensor and its relative strain. Usually this change in the electrical signal is produced by a change in resistance or capacitance. The parameter representing the sensitivity of the device is the Gauge Factor (GF) that can be calculated using Equation 8 or Equation 9 for resistive-type or capacitive-type strain sensors respectively:

$$GF = \frac{\left(\frac{\Delta R}{R_0}\right)}{\varepsilon} \quad (8)$$

$$GF = \frac{\left(\frac{\Delta C}{C_0}\right)}{\varepsilon} \quad (9)$$

It is possible to increase the sensitivity by decreasing the density of the percolation network, as in the case of CNTs-polymer strain sensors, however, this also causes a decrease in the maximum stretchability of the device. Many studies in literature have reported this correlation between gauge factor and stretchability, revealing a partial trade-

Table 1 Performance of recently published studies on strain sensors

Reference	Resistive/Capacitive	Materials	Stretchability (%)	GF
This study	Resistive	CNTs-Ecoflex	100	38.7
[102]	Resistive	CB-PDMS	30	29
[104]	Resistive	ZnONWs-PDMS	50	114
[43]	Resistive	AgNWs-PDMS	70	2-14
[105]	Resistive	CNTs-PDMS	280	0.82
[106]	Resistive	CNTs-Ecoflex	500	1-2.5
[83]	Capacitive	CNTs-silicone	100	0.99
[85]	Capacitive	CNTs-Dragonskin	300	0.97

It is evident how capacitive strain sensors generally possess a lower GF when compared to resistive-type sensors, due to their upper theoretical limit of GF = 1 [83, 85].

2.2.3.3 Hysteresis

Hysteresis takes place in elastic materials after repeated stretching cycles where different amount of stress is applied on the sensor. As the device return to its original position after loads of different entity have been applied, the length would not match exactly the initial length. This could lead to irreversible degradation of the sensor sensitivity with repeated usage and application of dynamic loadings. Normally, capacitive sensors possess a better behavior in terms of hysteresis when compared to the resistive-type [43, 85]. This could be easily explained as the change in length of a sensor due to hysteresis is more relevant then the change in thickness. As the capacitive-type sensors mainly rely on the distance *d* between the electrodes, represented by the thickness of the dielectric layer, they are not heavily affected by hysteresis. On the other hand, resistive-type sensors would be sensible to hysteresis as the resistance of the conductive trace could change due to an increase in length. Hysteresis effects can be worsened if the adhesion between the conductive trace and the polymer matrix is not strong enough. Slippage of nanomaterials when stretched would continuously change the sensor microstructural configuration leading to inconsistent results. This is mainly the case for CNTs-polymer nanocomposites due to their low interfacial bond strength. Conversely, another 1D nanomaterial, AgNWs, requires a low interfacial adhesion, otherwise friction between the matrix and the metallic nanomaterial could lead to buckling or fracture of these components.

2.2.3.4 Durability

Stretchability and sensitivity are considered the most importance parameters when evaluating the performance of a device. However, a sensor could show promising results in terms of both these parameters but failing in being consistent for repeated tests. Failure to achieve the same results over time is related to durability issues. Due to the repeated bending and stretching cycles that a sensor undergoes during its life, the mechanical and electrical properties can degrade over time. Previous studies have reported how buckling of the conductive component and irreversible deformation of the substrate are the main causes of inconsistent results [43, 91]. 1D carbon nanomaterials, CNTs, for example, behave better than their 0D counterpart (CB) due to their proven elastic behavior.

2.2.3.5 Response and Recovery Time

Response and recovery time are two important parameters to be considered when timely strain quantification is needed, for example for high frequency stretching cycles of short duration. Response and recovery time represent the amount of time that passes between the stress is applied and removed, respectively. Due to the viscoelastic property of polymers [43] there is a certain delay before the strain sensor responds to the strain with an electrical signal. Same applies to the recovery time, where the conductive network is restored to the initial state with a certain delay, depending both on the filler type and the nature of the substrate [105].

2.2.3.6 Linearity

Once the sensor has reached the steady-state behavior, the linearity parameter expresses how closely the strain-sensing trend resembles that of a straight line. The more linear the sensor, the easier becomes the calibration process and the generalization of the behavior of the sensor for a certain strain range. Many studies in literature reports how it is hard to fabricate sensors possessing high stretchability and sensitivity and a good linear behavior at the same time. Capacitive sensors are notable more linear, but they possess great limitations in terms of sensitivity (GF < 1). On the other hand, resistive-type sensors can reach high values of GF but are mostly affected by a non-linear behavior or limited stretchability.

2.2.4 Applications

Strain sensors can be used in a variety of different applications due to their high versatility. As the world population is slowly again with time, health monitoring for elderly patients has become a pressing need for hospitals. Specifically, being able to transfer this monitoring to their house making use of remote daily monitoring would help reduce the costs that have to be sustained on both parts and provide more comfortable solutions. It is then evident how strain sensors could find their perfect application in gait monitoring or fall prevention, especially if seamlessly integrated into daily clothes or specific garments. The ease of integration and the current trend toward miniaturization of these sensors is helping to make this goal more easily achievable and affordable at the same time [43, 84, 85, 91, 97, 99, 102, 103, 105-108].

The ability of these sensors of accurately discern between pressure and stretching has made them also an interesting candidate for guidance and monitoring of soft robots, as it is presented hereafter in this dissertation [42].

Being able to tailor the specific performance of the sensors depending on the type of conductive components and substrate, allows almost infinite possibilities depending on the usage. In certain cases, as it could be that of structural health monitoring, larger strains need to be detected, which do not require an extremely high sensitivity [85, 97, 99]. On the other hand, the same use of these sensors as health monitoring tools, if applied to pother anatomical areas could require a higher degree of sensitivity, compromising its ultimate stretchability.

In the case of applications of these sensors to soft robots, it is normally preferable to have a clear decoupling between pressure applied and stretching or bending induced by a certain curvature. Thus, the conductive filler needs to be chosen appropriately [109]. Highly sensitive strain sensors find their usage in more specific medical applications: they can indeed identify slight motions such as breathing, tissue swelling, or even phonation [84, 102, 110]. Such sensors are also useful to monitor sports activities of athletes [102, 105, 106].

The sharp rise in the use of VR technology and interaction between humans and machines have also created a new opportunity for strain sensor in the field of gesture recognition and remote control. Smart glove systems based on strain sensors have already been presented in many studies in literature [43, 82, 85, 105].

Lastly, as anticipated before, strain sensors could be integrated with soft robots to monitor their motion or sense the surrounding. The creation of an artificial skin covering the body of the robot would provide him with a perception sense based on strain sensing [111, 112].

2.3 Fractals and Serpentine Design

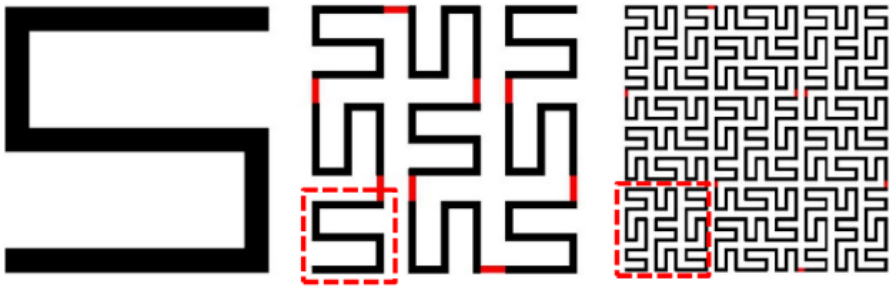

Figure 9 First, second and third order Peano curves [113]

The great variety of patterns, as they range from simple lines to more complex geometrical structures, guarantees almost complete freedom to tailor the design to a specific application. These curves can be seen as one-dimensional springs, on a mechanical point of view [113]. These Moreover these designs can be realized in a way that can accommodate strains in every direction, axial, biaxial or radial.

Lu *et al.* carried out a meticulous study on the influence of each geometrical parameter of serpentine patterns, in order to determine a rule of thumb when designing fractals. Their study merely focuses on this shape, but the concept could be easily extended to other patterns making the necessary modifications. The first important parameter that needs to be considered is the width-to-thickness ratio that expresses the tendency of a serpentine pattern to produce out-of-plane buckling. As pointed out in Section 2.2, buckling of

nanomaterials could degrade the performance of the device after repeated stretching/bending cycles. Consequently, in order to have full in-plane deformation of these curves, their width-to-thickness ratio should be small [114].

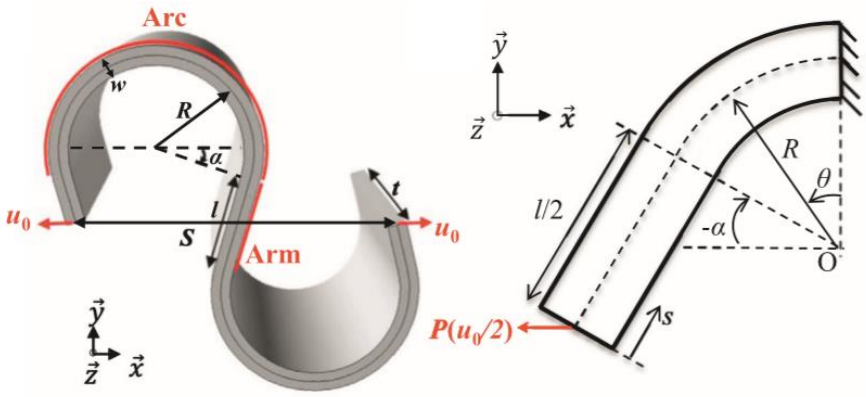

Figure 10 Serpentine geometrical parameters [114]

Fig. 10 provides an overview of the different geometrical parameters that uniquely defines the horseshoe shape. The straight segment between arcs depicted in Fig. 10 is the arm of the horseshoe, with length *l*. The other four geometrical parameters involved are the width *w*, the radius of curvature *R*, the arc angle α and the thickness *t*. It is demonstrated that serpentine patterns with large *l*/*R*, large α and small *w*/*R* have a better response when stretched, allowing a more homogeneous deformation when deposited, printed or transferred to a substrate and are also more mechanically reliable [114]. These parameters however should be considered in a context of practical limitations such as design constraints. While it is true that incrementing *l*/*R* to high values would enhance the mechanical properties of these patterns, the ribbons would ultimately end up overlapping.

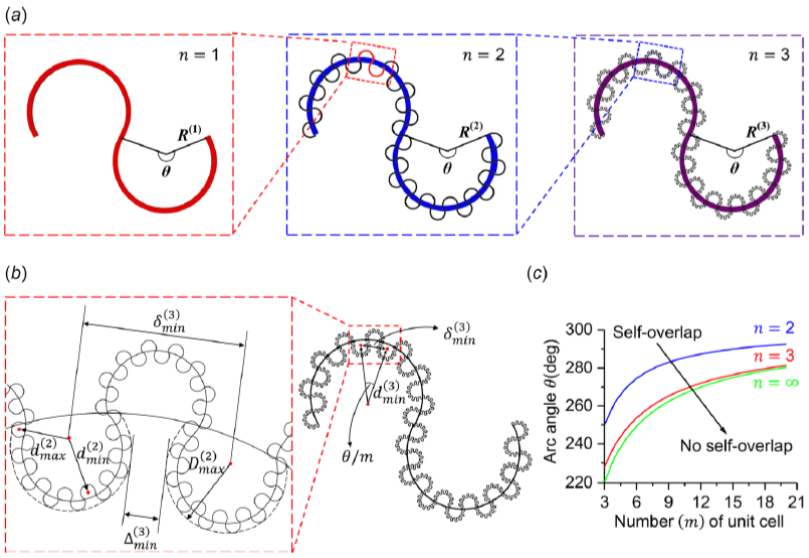

Figure 11 Horseshoe patterns with different orders and self-overlap critical point [115]

These fractals patterns greatly change their shape when stretched. Horseshoe or serpentine patterns tend to straighten when undergoing deformation, approaching the shape of a linear segment, which is never achieved before fracture of the pattern. When undergoing the shape-change deformation, these patterns respond both with a linear and a nonlinear fashion. Their response is greatly influenced by the substrate they are encapsulated in as that determines the overall stretchability. However, especially in case of a particularly soft silicone substrate, a good understanding of the behavior of freestanding serpentines could help predicting the overall mechanical performance of strain sensors.

Zhang *et al.* carried out a theoretical study on the non-linear response of horseshoe microstructures, based on the mechanism of ordered unraveling. The results indicate a substantial increase of elastic stretchability when employing horseshoe patterns and they have been validated with FEA analysis and experiments. It is demonstrated how structures designed on high-order fractals can be tuned in their mechanical behavior by varying the

geometrical parameters employed in their design. Moreover, the model they have presented could be fitted to other type of patterns, extending this study to the majority of fractal patterns. This gives great freedom in terms of geometry and allows to predict their non-linear behavior when undergoing mechanical stresses [115].

Fractal designs and serpentine patterns have found a critical application in the fabrication of strain sensors for wearable healthcare monitoring systems. The parallel development of fabrication techniques able to produce extremely thin and detailed electronic systems greatly benefited from the exploitation of fractal patterns.

Their major application resides in the fabrication of epidermal electronics [116]. These devices could be miniaturized both in planar area and thickness, in a way that they can be attached to the skin without creating any discomfort to the person wearing them. Moreover. these fractal structures give the device an extremely compliant behavior, following any deformation of the skin, such as stretching, bending and twisting. Such devices are able to couple to the skin effectively by means of Van der Waals forces alone (Fig. 12).

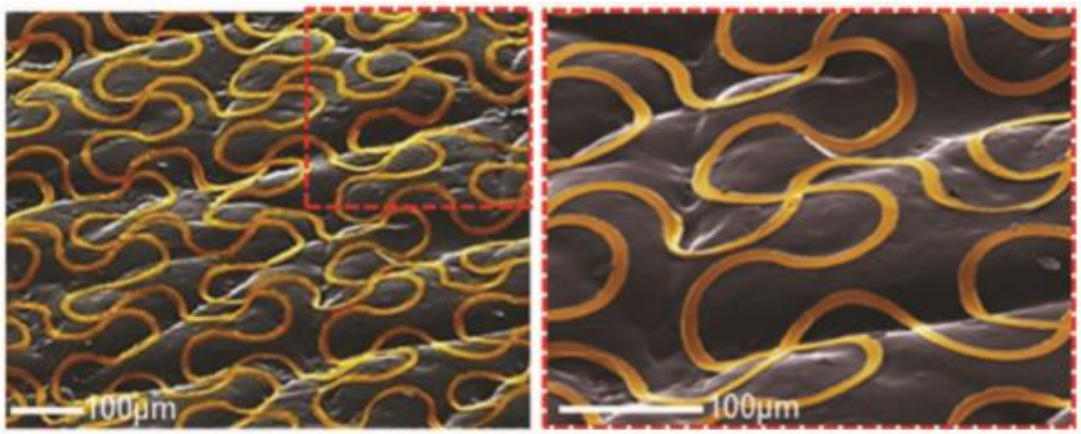

Figure 12 SEM images of an epidermal electronic device laminated on the skin [117]

Epidermal electronics can also be fabricated to be insensitive to moisture and water making them practical for daily usage. Fig. 13 shows how epidermal electronic devices can be fabricated using nano dimensional electronic components where serpentine traces are used as interconnects and antennae.

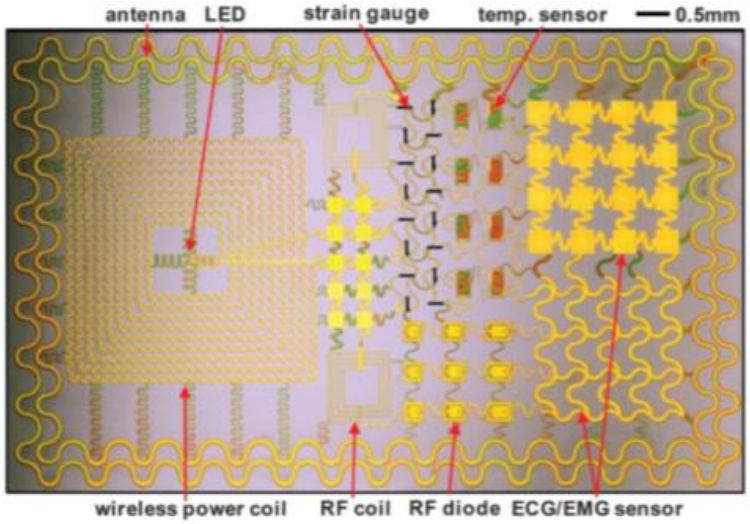

Figure 13 Epidermal electronic device employing fractal patterns [116]

CHAPTER 3. MATERIALS AND METHODS

3.1 Strain Sensor

3.1.1 Sensor Design

The strain sensor is designed using AutoCAD 2019 (Autodesk). The geometry of the sensor has been optimized according to the findings from Lu *et al.* [114] work on the influence of geometrical parameters on the final mechanical properties of serpentine patterns. Serpentines having large arc angle, large length-to-radius ratio and small width-to-thickness ratio have better performances. Therefore, a width of 1 mm and an arc angle of 270° have been selected as design parameters.

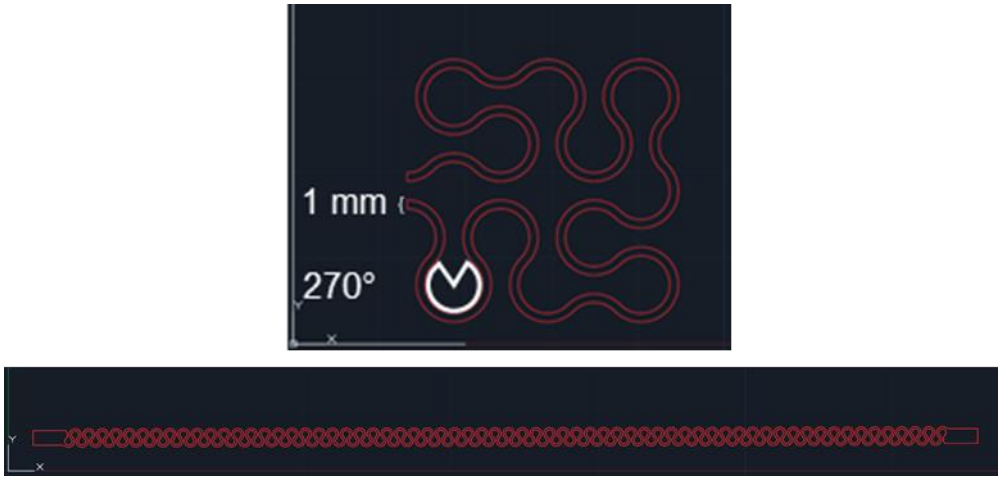

Figure 14 Strain sensor (top) and stretchable connectors (bottom) CAD design

3.1.2 Sensor Fabrication

A glass slide is used throughout the whole fabrication process to provide support when depositing the materials. The glass slide is first covered with a polyvinyl alcohol (PVA)

film that is used to avoid contact between the elastomer being deposited and the bare glass. Due to the stickiness of the substrate, having direct contact between these materials would make particularly difficult the removal when transferring the sensor. The PVA film represents a good choice to be used as substrate for the elastomer deposition, as it can be easily removed under flowing water thanks to its great solubility.

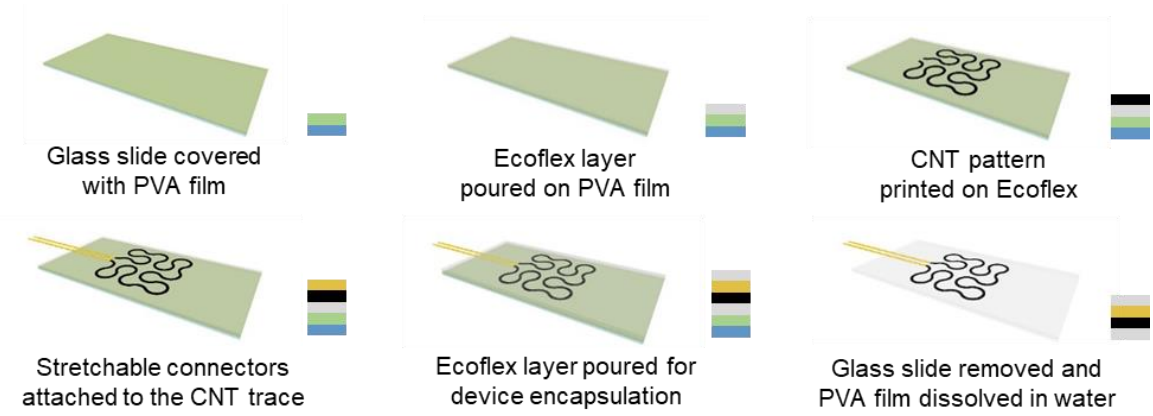

Figure 15 Schematic illustration of the strain sensor fabrication process

The material used as substrate for the strain sensor is a platinum-catalyzed silicone (Ecoflex 00_30, Smooth-On Inc.). The Ecoflex 00_30 substrate is prepared by mixing the two separate components provided by the supplier, the base (component A) and the curing agent (component B). These two components are mixed in a 1:1 weight ratio and then stirred continuously for 2 min to create a homogeneous formulation, following the supplier guidelines. As the desired overall thickness of the sensor was around 1mm, the PVA surface was covered with a small amount (3g) of the silicone formulation. Due to the long curing time of silicone, the elastomer successfully spread over the whole surface without leaving voids. In the rare case of bubble formation after pouring the formulation on the

substrate, a vacuum chamber is used to remove these air voids and create a homogeneous silicone layer. After deposition, the substrate is let cure for 4 hours at room temperature.

Figure 16 Ecoflex 00-30 Part A and B and Slo-Jo silicone cure retardant

After the curing process of the substrate is over, screen printing is used to deposit the sensing component on the substrate. Screen-printing is a low-cost high-throughput manufacturing technique that allows the deposition of inks or powders on a substrate selectively controlling where material is being deposited by means of a shadow mask.

Figure 17 Screen-printing experimental setup

The shadow mask is usually a sheet of stainless steel that include a “window” of cut-out steel, where the material can pass through and be deposited over the underlying

substrate. The ease and versatility of this technique resides in the customization of the shadow mask depending on specific needs of geometry or thickness of the mask, which also influences the thickness of the printed trace. In our case the shadow mask was custom realized using a femtosecond laser cutter (Optec WS Flex). Since this laser cutter works at high resolution, there was no need to keep any tolerance in fabricating the stencil, so the pattern used to realize the shadow mask is the same as the one used for sensor design in section 3.1.1.

Figure 18 Optec femtosecond laser micromachining system

The conductive material employed for the study is OH-functionalized carbon nanotubes (Nanostructured & Amorphous Materials Inc.) having a diameter of 20-30 nm, length of 5-20 μm and a purity of 95%. This type of CNTs have been chosen over other kind of functionalization due to their good compatibility with the Ecoflex silicone substrate.

Figure 19 OH-functionalized MWCNTs

Following the deposition of the CNT trace on the Ecoflex substrate, stretchable connectors are attached to the extremity of the trace electrically linking the sensor to the PCB. Stretchable connectors are microfabricated in a controlled cleanroom environment, following the steps that have been summarized in Fig. 20.

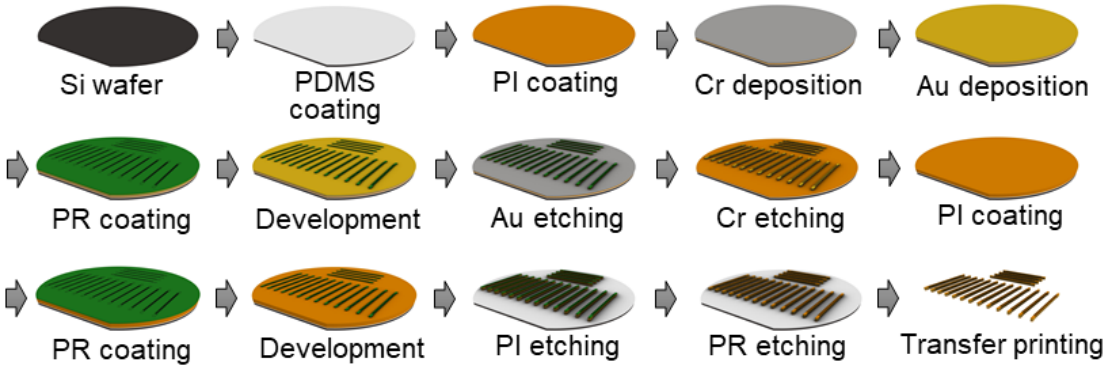

Figure 20 Stretchable connectors microfabrication process

Once the stretchable connectors are successfully removed from the silicon wafer and ready to transfer, they undergo a similar encapsulation as the one that have been performed on the strain sensor. Solaris (Fig. 21) is the elastomer being used in this case, due to it lower viscosity (1200 cps vs 3000 cps of Ecoflex) that allows an easy spreading process over the

miniaturized connectors, considerably more fragile than the thicker strain sensor fabricated before.

Figure 21 Solaris Part A and Part B

To bond the stretchable connectors to the CNT trace, a stretchable Ag ink (Namics, XE184E) is used, specifically tailored for applications that need enough bonding strength and stretchability. The ink is dispensed on the junction using a syringe and then cured on a hot plate at 70 °C for 30 minutes. Once the junction is made, a top layer of Ecoflex is poured to encapsulate the sensor. A different formulation is used for the top layer when compared to the bottom layer explained before. For the top layer a 4% in weight of silicone cure retardant (Slo-Jo, Smooth-On Inc.) is added to component B before this is mixed to component A. The mixture is stirred for 1 minute and then component A is added. The mixture is stirred once again for 1 minute and then 3g of the silicone formulation are poured on the sensor. The reason for the addition of Slo-Jo relies on its properties as a retardant agent for the curing process. Allowing to extend the curing time of the top layer by additional 2 hours allows the silicone to better penetrate inside the voids left in the screen-printing process between CNTs. The silicone molecules act as fillers between CNTs and create a more uniform trace that would deform more homogeneously than if these voids

wouldn’t have been filed. It is indeed not rare to see slipping between individual nanotubes once strain sensors are stretched. On the long term such slipping could lead to a deterioration of the sensing properties of the device or lost in consistency.

After 8 hours of curing at room temperature the device is ready for detachment from its original glass substrate. A metal blade is used to cut out the sensor from the surrounding Ecoflex area and then the sensor is peeled off from the underlying PVA film. If the peeling process results difficult, due to Ecoflex stickiness, the metal blade could be used to cut the PVA film as well, that is then dissolved by washing thoroughly the back of the sensor under flowing water for 5 minutes.

The resulting strain sensor shows excellent elastic properties when stretched both uniaxially and radially, as shown in Fig. 22 (left). The microfabricated stretchable connectors, that are similarly encapsulated in silicone, show comparable elasticity in Fig. 22 (center), thanks to the exploitation of a linear serpentine pattern. The outcome of the strain sensor fabrication has been verified using optical microscopy (VHX-600 Digital Microscope, Keyence) and scanning electron microscopy (SU8230, Hitachi) and the results are reported in Fig. 22 (right). Thanks to the images obtained via digital optical microscopy it is possible to verify how the CNT sensing trace was placed in the neutral mechanical plane, sandwiched evenly between the two Ecoflex layers, guaranteeing uniformity in the sensing behavior when stretching, bending and touching objects.

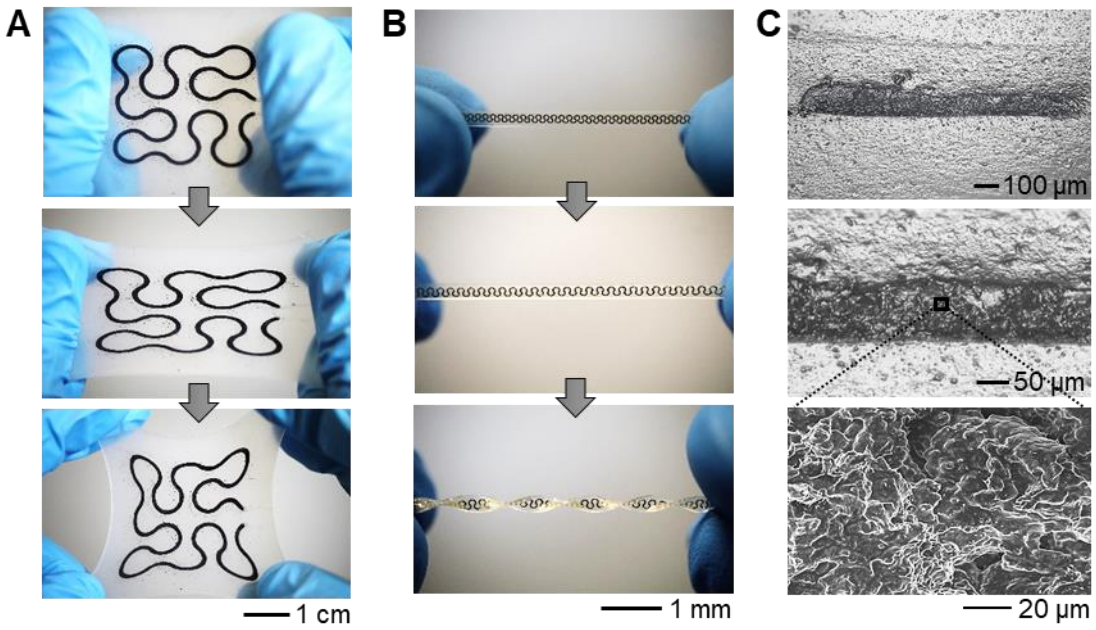

Figure 22 Fabrication of the strain sensor. (**A**) Strain sensor at rest (top), uniaxially stretched (middle) and radially stretched (bottom). (**B**) Microfabricated stretchable connectors at rest (top), uniaxially stretched (middle) and twisted (bottom). (**C**) Digital optical microscope images of the cross-section of the strain sensor at different magnifications (top and middle) and SEM image showing the microstructure of the printed trace (bottom).

3.1.3 Finite Element Analysis

Finite element analysis (FEA) is the tool chosen to predict the behavior of the strain sensor when undergoing mechanical deformation. For the purpose of the study only its mechanical behavior has been modeled, while the electromechanical behavior has been characterized experimentally but not validated with simulated results. The software Abaqus FEA (Dassault Systèmes) has been employed in the study.

An approximation has been done in modeling the strain sensor: considering the marginal impact of the CNT trace in the overall strain sensor mechanical properties, the sensor has been modeled as homogeneous in composition.

The following values have been used for Ecoflex 00_30 when modeling our system:

- Mass density: 1.07 x 10^{-9} kg/m^3
- Poisson ratio: 0.49 (estimation for rubber-like materials)

The Young modulus E is instead calculated directly from experimental data. The Mark-10 ESM303 tensile stretcher is used to gather data of applied force and relative strain of the sensor. The relative stress applied on the sensor (MPa) is calculated dividing the value of the force in N by the cross-sectional area in mm^2.

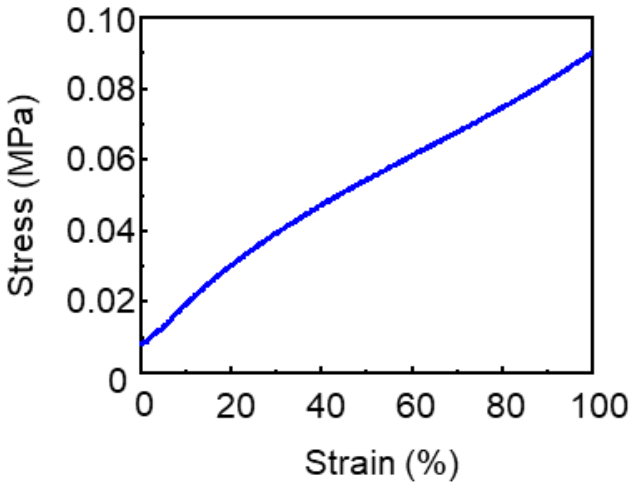

Figure 23 Stress-strain curve for uniaxial tensile test

According to the stress-strain curve (Fig. 23) the elastomer has been modeled as an hyperelastic material and the same stress-train data are loaded into Abaqus. Hyperleastic materials are modeled according to specific energy potential functions. In this case, the coefficients of the Ogden third order polynomial function for energy potential are calculated directly from the experimental stress-strain curve.

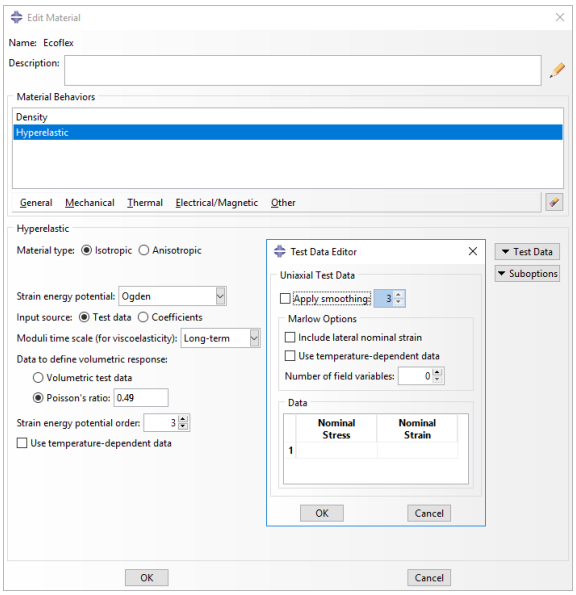

Figure 24 Specification of material's properties on Abaqus

A dynamic explicit method, with equally spaced stretching steps has been used in the simulation, guaranteeing a constant-rate deformation from start to end. For uniaxial stretching, it has been decided to set as boundary conditions a symmetric deformation along the x axis (U1) of 16 cm for each side of the sensor, while keeping null the deformation along y (U2) and z (U3). In doing so, the resulting elongation of the overall structure is equal to 100% of the initial length of the sensor (32 cm). A boundary condition a null rotation of each node (UR1, UR2, UR3) of the bottom and upper faces (silicone layers) was also set

Uniaxial stretching

- BC1 (applied on left face):
    - U1 = 16
    - U2 = 0
    - U3 = 0

- BC2 (applied on right face):
    - U1 = - 16
    - U2 = 0
    - U3 = 0
- BC3 (applied on top face):
    - UR1 = 0
    - UR2 = 0
    - UR3 = 0
- BC4 (applied on bottom face):
    - UR1 = 0
    - UR2 = 0
    - UR3 = 0

For biaxial stretching the same conditions previously described for uniaxial stretching were set, adding a symmetrical stretching condition along the y for the back and front faces of the strain sensor. Moreover, the condition U2 previously set null in BC1 and BC2 is now removed, since redundant.

Biaxial stretching

- BC1 (applied on left face):
    - U1 = 16
    - U3 = 0
- BC2 (applied on right face):
    - U1 = - 16

    - U3 = 0

- BC3 (applied on front face):
    - U2 = 16
    - U3 = 0
- BC4 (applied on back face):
    - U2 = - 16
    - U3 = 0
- BC5 (applied on top face):
    - UR1 = 0
    - UR2 = 0
    - UR3 = 0
- BC6 (applied on bottom face):
    - UR1 = 0
    - UR2 = 0
    - UR3 = 0

Due to the excellent properties of Ecoflex as a substrate for stretchable electronics very low values of strain for large deformations were predicted and then successively confirmed by experimental findings.

3.1.4 Characterization Techniques

3.1.4.1 Electromechanical Testing

The strain sensing performance of the sensor has been tested for different mechanical solicitations, linear, step and cyclic stretching. The setup employed for the electromechanical testing is reported in Fig. 25.

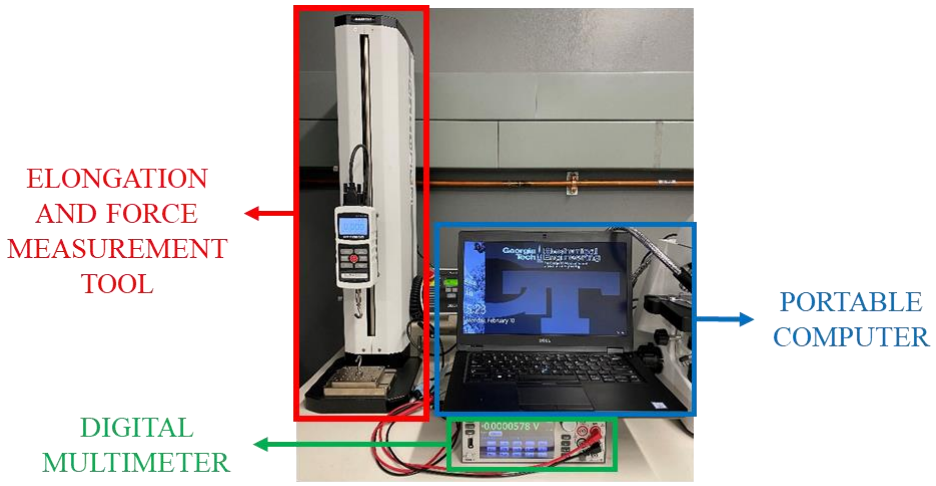

Figure 25 Experimental setup for electromechanical testing

The setup consists of a mechanical stretcher and force gauge (ESM303, Mark-10), a digital multimeter (DMM7510, Keithley) and a portable computer. The mechanical stretcher is used for uniaxial tensile test of the sensor, while the digital multimeter is connected to the stretchable connectors coming out of the encapsulated sensor, to keep track of the change in resistance when the device gets stretched. The portable computer simultaneously gathers data from the digital multimeter and the mechanical stretcher and is used for further processing.

Different parameters are used on the ESM303 depending on the type of test being carried out. For linear stretching:

- LO Limit: 0mm (starting point for elongation)
- HI Limit: 32mm (ending point for elongation)

- HI Dwell: 20s (time to wait at HI position)
- Speed UP: 100mm/min (elongation rate)

When carrying out step stretching, it has been decided to keep the sensor stretched at incremental steps of 10% strain for 20s. In order to do so a new parameter was introduced.

- HI Dwell: 20s (time to wait at HI position)

On the other hand, two more parameters needed to be added and the Speed UP to be modified when performing cyclic stretch tests:

- Cycles: 500 (number of cycles)
- HI Dwell: 5s (time to wait at HI position)
- Speed UP: 400mm/min
- Speed DO: 400mm/min (speed when coming back at LO position)

The digital multimeter is set up on the 2-wire resistance measurement configuration, with different NPLC values (aperture time), depending on the test performed. The NPLC is a parameter that correlates with the reading rate (samples/s) and defines the resolution of the measurement. The higher the value of the aperture time, the lower the number of readings per second. Due to the different length of each experiment, different values for the NPLC were set up, to have a reasonably detailed experiment. For:

- Linear stretching: NPLC = 1
- Step stretching: NPLC = 1
- Cyclic stretching (500 cycles): NPLC = 10

3.1.4.2 Digital Optical Microscopy

A Keyence VHX-600 Digital Microscope (Fig. 26) has been used to image a cross section of the strain sensor and provide information about the outcome of the fabrication process. As it is evident from Fig. 22C (top and middle), the fabrication process aimed to sandwich the CNT trace in between the two silicone layers was successful and the trace also appears to have been uniformly deposited along its width.

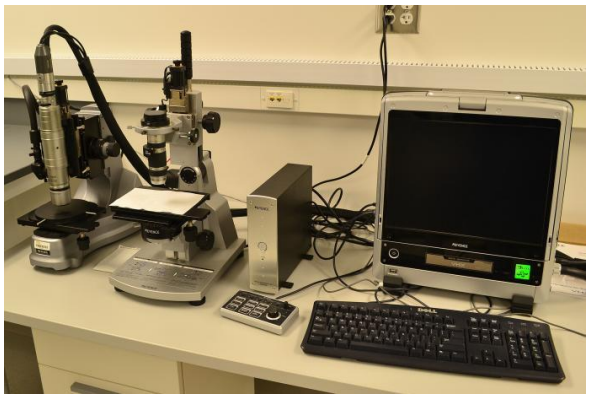

Figure 26 Keyence VHX-600 Digital Microscope

3.1.4.3 Scanning Electron Microscopy

Scanning electron microscopy (SEM) is used to image the cross section of the train sensor at a higher magnification than that used for digital microcopy. The goal is to provide the reader with a representation of the microstructure of the screen-printed trace to show the interpenetration of silicone in the CNT printed trace. This allows the CNTs to follow the deformation of the substrate, avoiding any slippage of nanotubes during the stretching process, that would irreversibly alter the conductivity of the network.

Figure 27 Hitachi SU8230 Scanning Electron Microscope

3.2 Electronic System

3.2.1 Electronic Module Design

The data acquisition system for the strain gauge sensor includes a Bluetooth Low Energy (Bluetooth 4.2 protocol) microcontroller (nRF52832, Nordic Semiconductor), integrated with a two-channel 24-bit analog-to-digital converter front end (ADS1292, Texas Instruments), with the inputs configured as a Wheatstone bridge to measure changes in resistance across the inputs. The data acquisition device is powered by a single lithium polymer battery. The ADC simultaneously samples at 125 samples per second on both channels, and the data are transmitted wirelessly to an Android tablet, where the data is plotted, recorded and analyzed. The wireless transmission latency is about 20 ms. The Bluetooth module can transmit consistently from up to 20 m of distance.

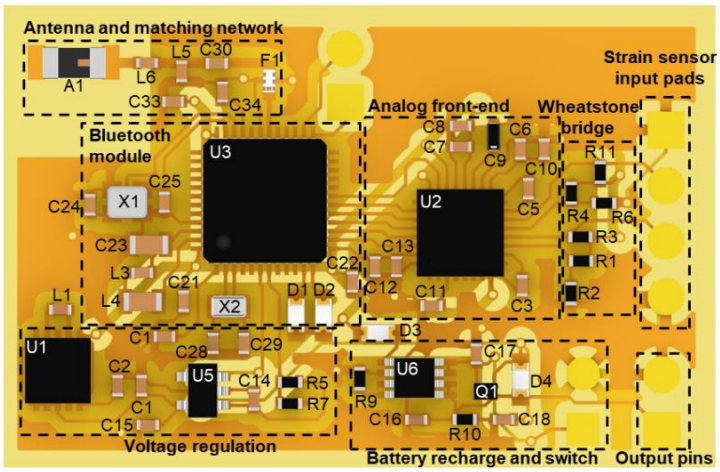

Figure 28 Top view illustration of flexible circuitry and electronic components

3.2.2 Electronic System Integration

The PCB is bonded to a previously cut microscope glass slide using double sided Kapton tape. As it is possible to see from Fig. 28, the power circuitry is activated by means of a dedicated switch. The switch position can be easily changed from ON to OFF from the outside of the robotic system thanks to one of the dedicated apertures in the 3D-printed plastic case. The integration of a switch allowed to have a more compact PCB design where the battery is integrated directly on board and it can be easily recharged using the output pins. These pins are easily accessible from the outside of the robotic worm as well thanks to another custom-made aperture.

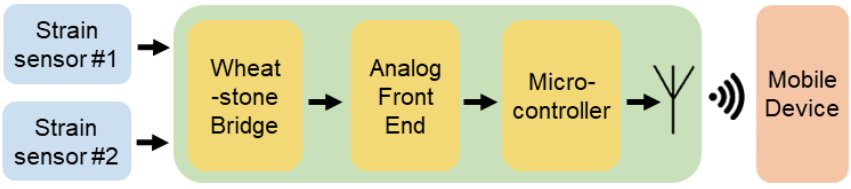

Figure 29 Schematic illustration of data acquisition, processing and communication

3.3 Soft Earthworm Robot

3.3.1 Robot Design

The major objective of the study is the monitoring of the locomotion of robotic systems enabling them of sensing capabilities in order to detect the surrounding environment. As already pointed out in the Introduction, of major interest is the study of earthworms' locomotion, since robotic systems that are inspired from them are widely used for environmental exploration.

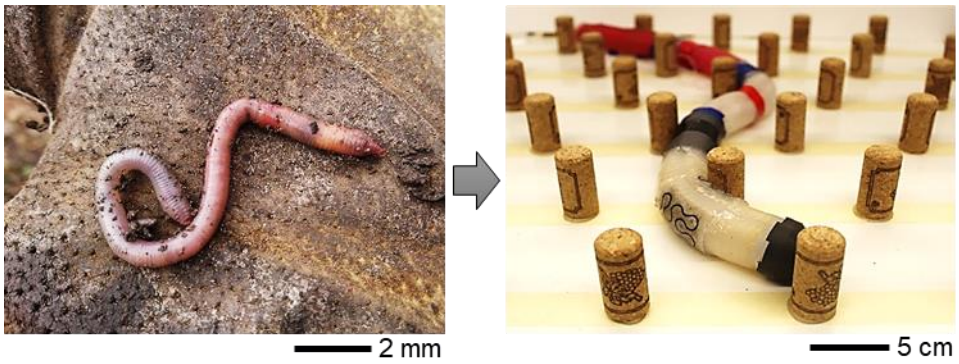

Figure 30 Bio-inspired robotic earthworm

The body of our robotic system is composed of several soft segments made of silicone material (Dragonskin, Smooth-on Inc.) joined using rigid connectors. A rigid tip is also used as the head of the robotic worm. Both the rigid connectors and the tip are 3D-printed using common plastic materials (PLA) since these components are only used as structural support for the system and do not need to perform any specific task.

The robotic worm is given the ability of stretching and bending thanks to a Kevlar thread that is mounted in between the two silicone layers and guarantees a homogeneous

deformation when the body of the earthworm is inflated. Inflation is performed by means of flexible pneumatic tubes that are connected to an external pneumatic control board.

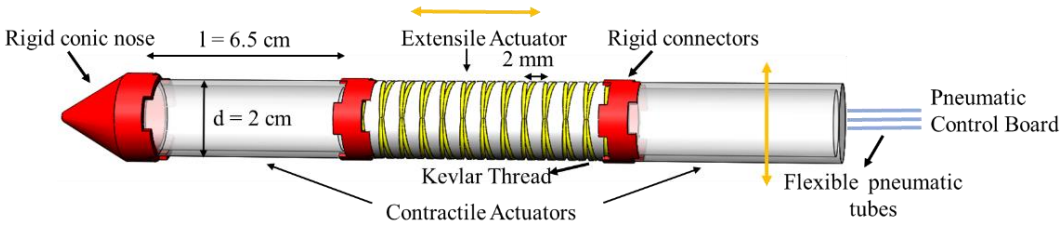

Figure 31 Schematic illustration of the soft robot

The dimensions of the strain sensor have been tailored to fit on both sides of the robot body allowing the placement of two sensors (one left and one right) per segment. The choice of using stretchable connectors to transmit the signal from the sensor allowed to encapsulate them as well on the body of the earthworm, providing a robust final design without any hanging component, that could potentially cause artifacts when gathering data from the device. In fact, in a prior prototype anisotropic conductive films (ACFs) were used but due to their impossibility to stretch with the earthworm body, they needed to remain outside the final encapsulation creating issues when handling the system. If encapsulated inside the body, on the other hand, their rigidity created stress concentration spots at the junction between the connectors and the CNT trace, resulting in a disconnection of the device when stretched.

The stretchable connectors on the other side are bonded to the PCB that is placed inside the 3D-printed plastic case. The case has been designed with three apertures for specific purposes:

- *Top large aperture*: stretchable connectors via for communication between the sensor and the PCB inside the case.
- *Top small aperture*: the switch that turns on and off the electronic circuit can be controlled by the outside without need to disassemble the robot.
- *Left side small aperture*: pins for battery recharge are allocated on the left side of the case and are in this way easily reachable when needed to be connected to the external battery charger.

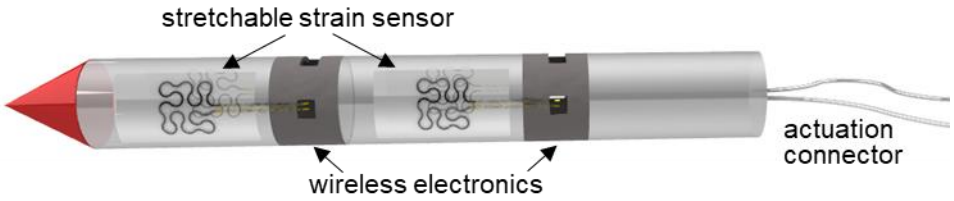

Figure 32 3D rendering of the integrated robotic system

3.3.2 Electronic System Integration

The strain sensors are encapsulated on the body of the earthworm using Solaris (Smooth-On Inc.) in a 1:1 ratio of component A and component B, following the guidelines provided by the supplier. First, 2g of Solaris are spread on the back of the sensor and the sensor is placed on its final location on one side of the worm's soft body. Thanks to the long curing time of Solaris, this approach allows to have a uniform curing process of the sensor on the robot body but at the same time, a faster curing method is applied on the sides to confine it and give the sensor more bonding strength on the sides and corners, where stresses are concentrated. Additional Solaris is spread along the sides using a wood spatula and a hot air gun is used to selectively cure the Solaris on the edges. Moving the air gun along the

side of the sensor at 2 cm from the surface for 5 minutes at 150°C guarantees a successful bonding. The action is repeated for each side of the sensor. Once the sensor on one side is bonded to the body, the same procedure is followed for the sensor on the opposite side.

Following the encapsulation of the sensors on the robot's body, the PCB is bonded to the rigid case to avoid any relative movement. In order to do so, we spread epoxy on the back side of the glass slide where the PCB is attached. Then the PCB is placed on the plastic supports inside the 3D-printed case and let cure at room temperature for 1 hour. The last step in the device integration process is the bonding of the charging pins to the side walls of the plastic aperture, once again to avoid any relative movement that could be source of failure for repeated locomotion cycles. Epoxy is once again used to bond the pins to the case and let cure for 1 hour at room temperature. Such procedure is repeated for each segment of the robot earthworm, where every segment consists of a soft actuator and a rigid case allocating the electronic module.

CHAPTER 4. RESULTS

4.1 Strain Sensor Electromechanical Performance

The strain sensor has been characterized according to the performance parameters highlighted in the Introduction. In order to have a reliable strain sensor for our robotic application, high stretchability, high sensitivity and consistency over time are needed.

In order to validate the experimental findings, a finite element analysis (FEA) simulation of the deformation expected from the strain sensor for a strain of 75% is first performed. When setting up the simulation on Abaqus FEA (Dassault Systèmes) an approximation in modeling the sensor has been made. The screen-printed CNT trace has limited thickness compared to the overall thickness of the strain sensor (<10%) and its mechanical behavior can't be modeled as that of a bulk material, since nanotubes aren't bonded together during deposition. Moreover, letting the top layer of Ecoflex 00_30/Slo-Jo cure for a longer time allowed the silicone to penetrate inside the voids of the printed trace, thus creating a nanocomposite layer having mechanical properties considerably different than that of CNTs. Consequently, it has been decided to model the CNT trace as made of silicone, being the mechanical properties of the substrate largely dominant over that of the sensing layer. It is possible to appreciate from Fig. 33 the exact correspondence between the simulation and the actual photo of the sensor undergoing deformation using a mechanical stretcher and force gauge (ESM303, Mark-10).

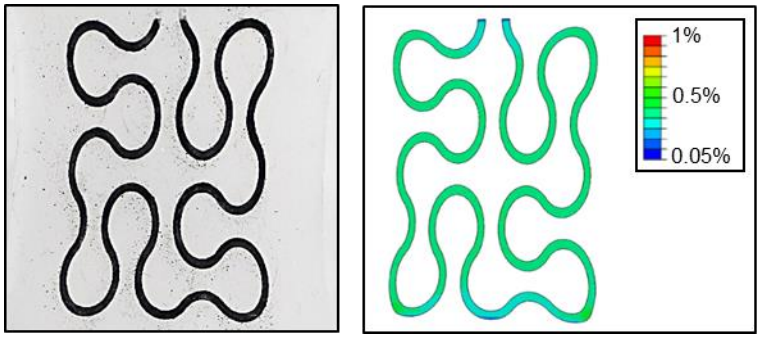

Figure 33 Strain sensor stretched at ε = 60% (left) and correspondent FEA simulation (right)

A similar FEA simulation has been carried out for the stretchable connectors. Since these connectors would not face the same stress, and consequently strain, of the strain sensor, they are only tested for a maximum strain of 60%. The results from the FEA simulation, reported in Fig. 34 below, shows how the maximum strain for these connectors remain under 1%, for a deformation of 60% the initial length.

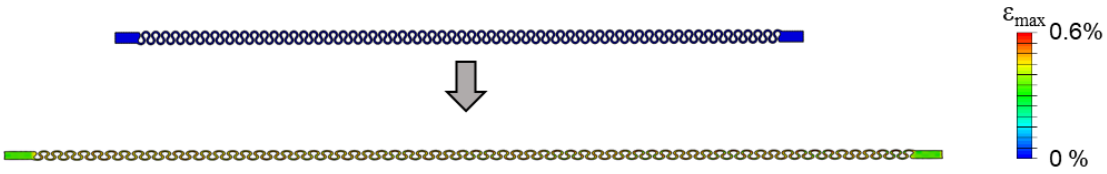

Figure 34 Stretchable connectors FEA simulation from 0 to 60% strain

The microfabricated stretchable connectors are used as carriers of the electrical signal generated by the strain sensor, that needs to be analyzed and transmitted to a mobile device. Considering their function, it is then needed to verify how these connectors change their intrinsic resistance when stretched, since this could jeopardize the final result, if considerably affecting the strain sensing performance. In order to do so, a stretchable connector is stretched to a 60% strain using the mechanical stretched already employed in

the study. ACFs are bonded to the leads of the stretchable connectors to allow for simultaneous monitoring of the resistance value when stretched. A total of 200 cycles from 0 to 60% strain were performed on the connectors, and the results are summarized in Fig. 35.

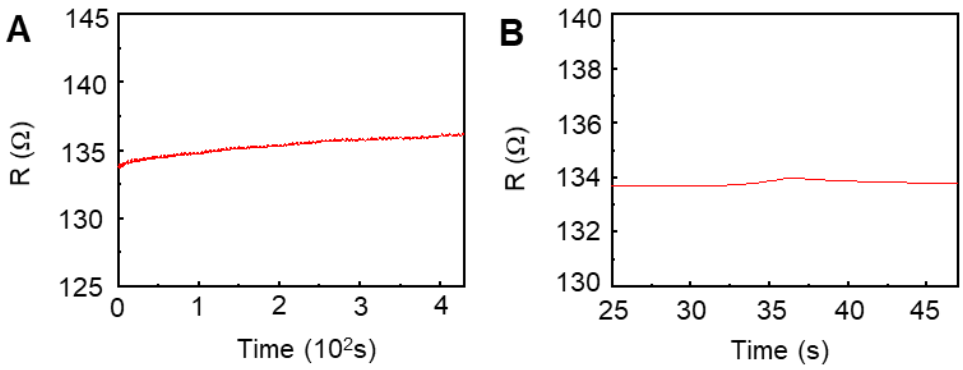

Figure 35 (**A**) Cyclic uniaxial tensile test for stretchable connectors (200 cycles). (**B**) Magnification showing a single stretching event

The stretchable connectors showed excellent stability in terms of intrinsic resistance, with a shift of only 2.7 Ω after 200 cycles of stretching, that is marginal considering the overall change in resistance of the strain sensor when performing its function.

The sensitivity of the strain sensor is then evaluated by measuring its change in resistance with increasing strain, clamping the stretchable leads to a digital multimeter and performing stretching. The sensitivity of strain sensors is usually defined by the adimensional gauge factor parameter (GF):

$$GF = \frac{\left(\frac{\Delta R}{R_0}\right)}{\varepsilon} \tag{8}$$

where ΔR is the relative change in resistance between the value R_0 at ε = 0% and the resistance measured at ε = 100%, and ε is the strain of the sensor. The strain sensor being developed find its application in soft robotic locomotion monitoring where it is required at least a stretchability of 60/70% to be able to follow the deformation of the robot body when bending. On the other hand, a high sensitivity is also fundamental to be able to distinguish between proprioception and exteroception. The fabricated strain sensor possesses a GF ~ 38.7, showing an excellent sensitivity for a range of strain from 0 to 100%. The behavior of the sensor with increasing resistance is shown in Fig. 36, that highlights a trend closely fitting an exponential fashion, with a value of $R^2 = 0.996$.

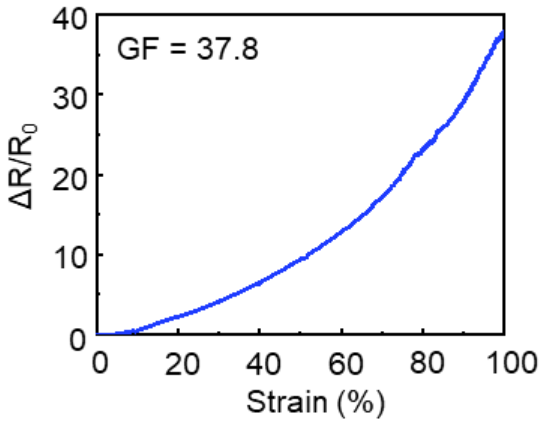

Figure 36 Strain sensor behavior for 0-100% range of uniaxial stretching

When evaluating the strain sensing response of the sensor, of particular interest for the purpose of the study was evaluating a possible shift in resistance if maintained at a certain elongation for a given time. Consequently, as reported in Fig. 37, a sequential step stretching test was performed, where 10% strains were followed by a 20s rest, with the sensor held at that strain, going from 0 to a 100% strain. As it is possible to appreciate from the results, the sensor showed excellent stability in terms of resistance when kept at a

constant strain value until ε ~ 80%. Relaxation deriving from the elastic nature of our substrate and consequent rearrangement of the CNTs in the printed trace can be observed after a 70% strain. However, considering the specific application of the sensor for robot locomotion, where such strains are not achieved, this result is given marginal importance.

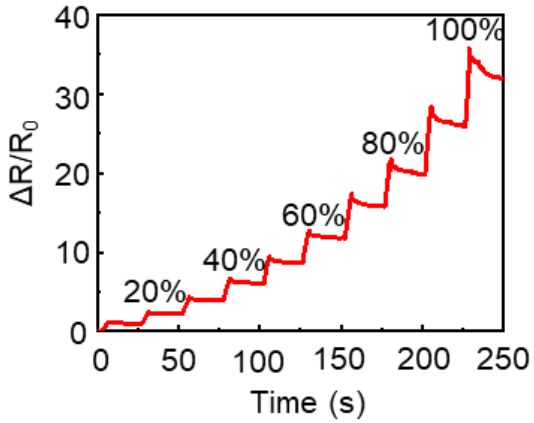

Figure 37 Incremental step stretching from 0 to 100% strain

In order to guarantee repeatability of the performance of the sensor, a cyclic stretching test from 0 to 100% strain has been performed for 500 stretching cycles. The graph reported in Fig. 38 shows how the sensor maintains its sensitivity throughout the whole experiment with marginal drift in the value of $\Delta R/R_0$ at $\varepsilon = 100\%$. The inset shows a detailed view of 50 cycles. The peaks relative to each of the 500 cycles have been identified and the mean have been computed giving a value of GF = 34.6 with a standard deviation $\sigma = 2.2$. More cyclic stretching tests have also been conducted when testing left and right bending of the robotic system and those are reported in the section below.

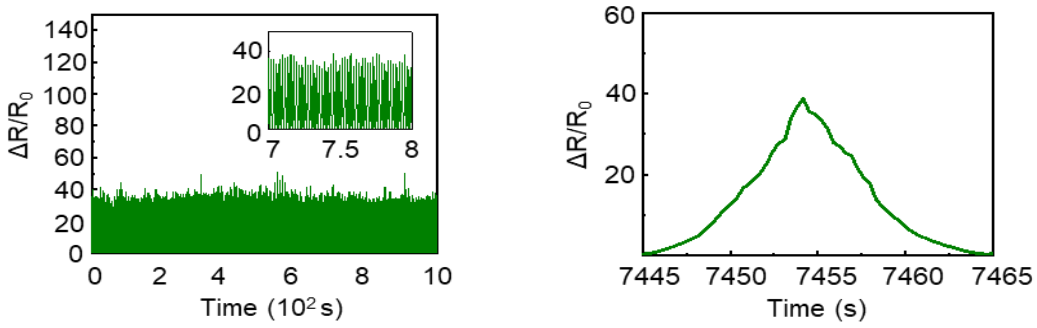

Figure 38 500 cycles of uniaxial stretching from 0 to 100% (left) and magnification of a single stretching event (right)

Moreover, it was considered valuable to understand the behavior of the sensor when continuously stretched at high frequency, in order to capture the behavior in both loading and unloading. The silicone substrate usually slows down the return to the initial value of resistance of the sensor, due its long relaxion times. As a result, what is seen when this happens is an asymmetric behavior in loading and unloading. However, the speed at which the deformation is performed (both in loading and unloading) can play a key role in determining the entity of such effect. Fig. 36 and Fig. 38 shows results from uniaxial tensile tests performed at different speed, 50 mm/min and 200 mm/min respectively. It has been already reported how after an 80% strain relaxation of the silicone substrate becomes evident. Fig. 38 includes a peak extracted from the cyclic test data, showing how the change in resistance between loading and unloading was instead symmetrical, leading to the conclusion that higher deformation speeds mitigate such phenomena.

4.2 Soft Robot Locomotion Detection

After the evaluation of the intrinsic electromechanical properties of the fabricated strain sensor, two of such sensors have been attached on the body of the soft robot, one on each side in order to have complementary information on its locomotion. As it has been already

stressed in the Introduction, the main purpose of the study was that of giving the soft robotic system the capability of both feeling its own movements and the encumbrance of its body (proprioception) and the ability of perceiving the surrounding environment and adjacent objects (exteroception).

The proficiency of the sensor in both proprioception and exteroception in demonstrated in Fig. 39. The soft robotic system has been tested in order to capture the response of the sensor to commonly experienced external stimuli. It is possible to appreciate from the first series of peaks (1) how the sensor provides alternate feedbacks on compression and elongation associated with right and left bending. Whenever the sensor on one side undergoes elongation and shows a steep voltage increase, the sensor on the opposite side shows a small bump, characteristic of the compression mode. This has also been verified with the sequence of peaks (2), where only left bending has been performed, isolating the compression peaks on the left sensor curve. In (3) the robot has been tested for simultaneous compression on both sides of the segment, with no actuation (3). The peaks numbered (4) are those associated with a vertical compression of the robot, with a pressure directed toward the ground applied on the plastic tip. Forward stretching, where both sensors are undergoing the same deformation, is characterize by similar voltage peaks in the both curves (5). These peaks give a ΔV that is positive with respect to the baseline, while those associated with vertical compression are instead negative with respective to the same baseline (4). The robot has also been tested for obstacles detection, showing characteristic peaks of lower intensity for pressure or touch on the sensor (6), when compared to bending (due to the entity of the deformation of the printed CNT trace).

Moreover, much lower peaks can be associated with vibration of the ground, that have been also simulated for completeness (7).

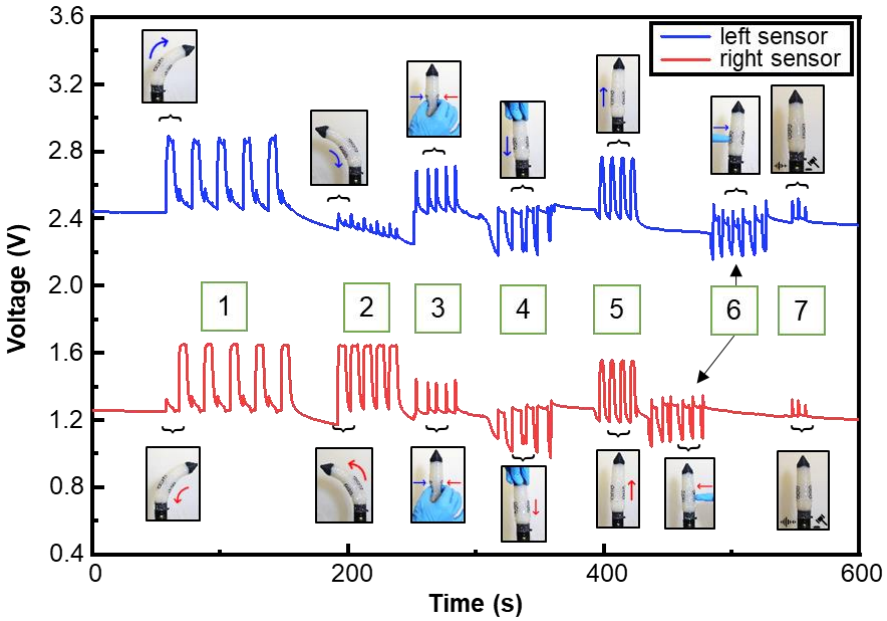

Figure 39 Device proficiency in proprioception and exteroception

Each segment of the soft robotic system has also been tested for cycles of both forward stretching and left/right bending. The results are summarized in Fig. 40. The reported graphs show consistency in the amplitude of the voltage peaks when the robot is stretching or bending. Moreover, magnifications have been included to grasp finer details about the locomotion detection. For forward motion, it is possible to appreciate how both the left and right sensor respond with the same timing to the internal stimulus, having identical voltage peaks and then suggesting an identical response due to simultaneous elongation of both the sides of the robot body. For left and right bending (bottom) in turn, it is evident how the voltage peaks associated with stretching are out-of-phase, since left and right bending moves are alternated. Moreover, it is possible to notice how both the right and left sensors

show a compression dip, a small voltage drop that can be associated with the corresponding compression of the sensor on one side when the other sensor is getting stretched.

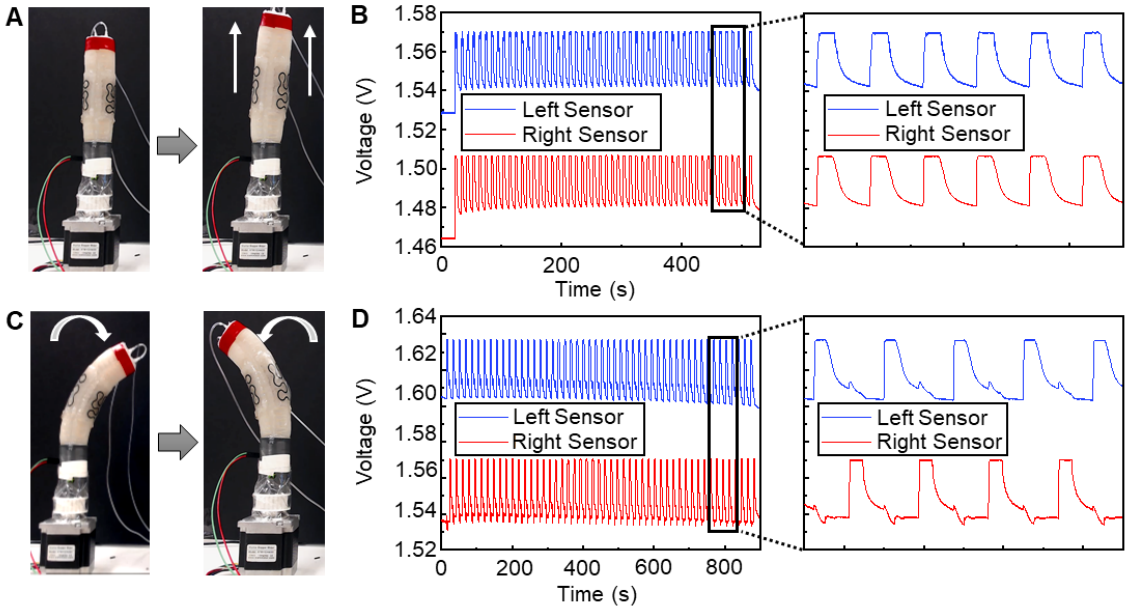

Figure 40 Earthworm robot locomotion detection

CHAPTER 5. DISCUSSION AND CONCLUSIONS

Here the fabrication of a nanocomposite strain sensor and relative electronic system is presented, and its successful integration of the body of a soft robotic earthworm for detection of its locomotion is explained. The high elasticity of the silicone substrate employed for the fabrication of the sensor guarantees an excellent compliance with the earthworm robot body for the whole range of movements that it could perform. Moreover, the high sensitivity of the CNT serpentine trace acting as sensing layer makes the device fully functional for detection of surrounding objects or external stimuli. The rearrangement of CNTs inside the silicone matrix after bending or stretching events proved to have only a marginal effect for the overall purpose of the study. Moreover, such effect becomes evident and should be taken into consideration only for values of strain > 70%, that are not achieved by the robot when performing locomotion. The choice of microfabricating dedicated stretchable connectors proved to be fundamental in eliminating the stress concentration issue that has been encountered when previously using flexible ACFs for electrical signal communication. Employing Bluetooth technology for data transmission makes the device wireless and paves the way for its integration in untethered robots that can be controlled remotely. The next phase of this study would in fact be closed-loop electronic system that would empower the robot of decision capability. The strain sensing device would provide real-time feedbacks to the robot that would then be able to change its locomotion direction, avoid obstacles or respond to external stimuli, thanks to the integration of an Arduino board. The work here reported constitutes a first step toward the

direction of fully automated robot locomotion based on strain sensing, that could find its most prominent application in the exploration of harsh environments.

REFERENCES

[1] S. Kim, C. Laschi, and B. Trimmer, "Soft robotics: a bioinspired evolution in robotics," *Trends Biotechnol,* vol. 31, no. 5, pp. 287-94, May 2013, doi: 10.1016/j.tibtech.2013.03.002.

[2] M. Porez, F. Boyer, and A. J. Ijspeert, "Improved Lighthill fish swimming model for bio-inspired robots: Modeling, computational aspects and experimental comparisons," *The International Journal of Robotics Research,* vol. 33, no. 10, pp. 1322-1341, 2014, doi: 10.1177/0278364914525811.

[3] Z. Ye, S. Régnier, and M. Sitti, "Rotating Magnetic Miniature Swimming Robots With Multiple Flexible Flagella," *IEEE Transactions on Robotics,* vol. 30, no. 1, pp. 3-13, 2014, doi: 10.1109/TRO.2013.2280058.

[4] S.-W. Yeom and I.-K. Oh, "A biomimetic jellyfish robot based on ionic polymer metal composite actuators," *Smart Materials and Structures,* vol. 18, no. 8, p. 085002, 2009/06/03 2009, doi: 10.1088/0964-1726/18/8/085002.

[5] H.-T. Lin, G. G. Leisk, and B. Trimmer, "GoQBot: a caterpillar-inspired soft-bodied rolling robot," *Bioinspiration & Biomimetics,* vol. 6, no. 2, p. 026007, 2011/04/26 2011, doi: 10.1088/1748-3182/6/2/026007.

[6] C. D. Onal, X. Chen, G. M. Whitesides, and D. Rus, "Soft Mobile Robots with On-Board Chemical Pressure Generation," in *Robotics Research : The 15th International Symposium ISRR*, H. I. Christensen and O. Khatib Eds. Cham: Springer International Publishing, 2017, pp. 525-540.

[7] M. Kovac, M. Fuchs, A. Guignard, J. Zufferey, and D. Floreano, "A miniature 7g jumping robot," in *2008 IEEE International Conference on Robotics and Automation*, 19-23 May 2008 2008, pp. 373-378, doi: 10.1109/ROBOT.2008.4543236.

[8] K. Hosoda, Y. Sakaguchi, H. Takayama, and T. Takuma, "Pneumatic-driven jumping robot with anthropomorphic muscular skeleton structure," *Autonomous Robots,* vol. 28, no. 3, pp. 307-316, 2010/04/01 2010, doi: 10.1007/s10514-009-9171-6.

[9] F. Li *et al.*, "Jumping like an insect: Design and dynamic optimization of a jumping mini robot based on bio-mimetic inspiration," *Mechatronics,* vol. 22, no. 2, pp. 167-176, 2012/03/01/ 2012, doi: https://doi.org/10.1016/j.mechatronics.2012.01.001.

[10] K. Y. Su, J. Z. Gul, and K. H. Choi, "A biomimetic jumping locomotion of functionally graded frog soft robot," in *2017 14th International Conference on Ubiquitous Robots and Ambient Intelligence (URAI)*, 28 June-1 July 2017 2017, pp. 675-676, doi: 10.1109/URAI.2017.7992792.

[11] M. Calisti *et al.*, "Design and development of a soft robot with crawling and grasping capabilities," in *2012 IEEE International Conference on Robotics and Automation*, 14-18 May 2012 2012, pp. 4950-4955, doi: 10.1109/ICRA.2012.6224671.

[12] B. S. Homberg, R. K. Katzschmann, M. R. Dogar, and D. Rus, "Haptic identification of objects using a modular soft robotic gripper," in *2015 IEEE/RSJ International Conference on Intelligent Robots and Systems (IROS)*, 28 Sept.-2 Oct. 2015 2015, pp. 1698-1705, doi: 10.1109/IROS.2015.7353596.

[13] Y. Wei *et al.*, "A Novel, Variable Stiffness Robotic Gripper Based on Integrated Soft Actuating and Particle Jamming," *Soft Robotics*, vol. 3, no. 3, pp. 134-143, 2016, doi: 10.1089/soro.2016.0027.

[14] T. Umedachi, V. Vikas, and B. A. Trimmer, "Highly deformable 3-D printed soft robot generating inching and crawling locomotions with variable friction legs," in *2013 IEEE/RSJ International Conference on Intelligent Robots and Systems*, 3-7 Nov. 2013 2013, pp. 4590-4595, doi: 10.1109/IROS.2013.6697016.

[15] M. Calisti, G. Picardi, and C. Laschi, "Fundamentals of soft robot locomotion," *J R Soc Interface*, vol. 14, no. 130, May 2017, doi: 10.1098/rsif.2017.0101.

[16] B. Trimmer, A. Takesian, B. Sweet, C. Rogers, D. Hake, and D. Rogers, "Caterpillar locomotion: A new model for soft-bodied climbing and burrowing robots," *Proceedings of the 7th International Symposium on Technology and the Mine Problem*, 04/02 0002.

[17] E. W. Hawkes, L. H. Blumenschein, J. D. Greer, and A. M. Okamura, "A soft robot that navigates its environment through growth," *Science Robotics*, vol. 2, no. 8, p. eaan3028, 2017, doi: 10.1126/scirobotics.aan3028.

[18] S. Seok, C. D. Onal, K. Cho, R. J. Wood, D. Rus, and S. Kim, "Meshworm: A Peristaltic Soft Robot With Antagonistic Nickel Titanium Coil Actuators," *IEEE/ASME Transactions on Mechatronics*, vol. 18, no. 5, pp. 1485-1497, 2013, doi: 10.1109/TMECH.2012.2204070.

[19] W. Hu, G. Z. Lum, M. Mastrangeli, and M. Sitti, "Small-scale soft-bodied robot with multimodal locomotion," *Nature*, vol. 554, no. 7690, pp. 81-85, 2018/02/01 2018, doi: 10.1038/nature25443.

[20] N. Taro and I. Tomohide, "Locomotion strategy for a peristaltic crawling robot in a 2-dimensional space," in *2008 IEEE International Conference on Robotics and*

Automation, 19-23 May 2008 2008, pp. 238-243, doi: 10.1109/ROBOT.2008.4543215.

[21] B. Kim, M. G. Lee, Y. P. Lee, Y. Kim, and G. Lee, "An earthworm-like micro robot using shape memory alloy actuator," *Sensors and Actuators A: Physical*, vol. 125, no. 2, pp. 429-437, 2006/01/10/ 2006, doi: https://doi.org/10.1016/j.sna.2005.05.004.

[22] A. J. Ijspeert, A. Crespi, and j.-m. Cabelguen, "Simulation and Robotics Studies of Salamander Locomotion: Applying Neurobiological Principles to the Control of Locomotion in Robots," *Neuroinformatics*, vol. 3, pp. 171-195, 09/01 2005, doi: 10.1385/ni:3:3:171.

[23] M. Luo *et al.*, "Slithering towards autonomy: a self-contained soft robotic snake platform with integrated curvature sensing," *Bioinspiration & Biomimetics*, vol. 10, no. 5, p. 055001, 2015/09/03 2015, doi: 10.1088/1748-3190/10/5/055001.

[24] T. Oshima, N. Momose, K. Koyanagi, T. Matsuno, and T. Fujikawa, "Jumping Mechanism Imitating Vertebrate by the Mechanical Function of Bi-articular Muscle," in *2007 International Conference on Mechatronics and Automation*, 5-8 Aug. 2007 2007, pp. 1920-1925, doi: 10.1109/ICMA.2007.4303844.

[25] K. A. Daltorio, A. S. Boxerbaum, A. D. Horchler, K. M. Shaw, H. J. Chiel, and R. D. Quinn, "Efficient worm-like locomotion: slip and control of soft-bodied peristaltic robots," *Bioinspiration & Biomimetics*, vol. 8, no. 3, p. 035003, 2013/08/27 2013, doi: 10.1088/1748-3182/8/3/035003.

[26] A. Menciassi, S. Gorini, G. Pernorio, and P. Dario, "A SMA actuated artificial earthworm," in *IEEE International Conference on Robotics and Automation, 2004. Proceedings. ICRA '04. 2004*, 26 April-1 May 2004 2004, vol. 4, pp. 3282-3287 Vol.4, doi: 10.1109/ROBOT.2004.1308760.

[27] G. Methenitis, D. Hennes, D. Izzo, and A. Visser, "Novelty Search for Soft Robotic Space Exploration," presented at the Proceedings of the 2015 Annual Conference on Genetic and Evolutionary Computation, Madrid, Spain, 2015. [Online]. Available: https://doi.org/10.1145/2739480.2754731.

[28] G. Soter, A. Conn, H. Hauser, and J. Rossiter, "Bodily Aware Soft Robots: Integration of Proprioceptive and Exteroceptive Sensors," in *2018 IEEE International Conference on Robotics and Automation (ICRA)*, 21-25 May 2018 2018, pp. 2448-2453, doi: 10.1109/ICRA.2018.8463169.

[29] J. Morrow *et al.*, "Improving Soft Pneumatic Actuator fingers through integration of soft sensors, position and force control, and rigid fingernails," in *2016 IEEE International Conference on Robotics and Automation (ICRA)*, 16-21 May 2016 2016, pp. 5024-5031, doi: 10.1109/ICRA.2016.7487707.

[30] K. Noda, E. Iwase, K. Matsumoto, and I. Shimoyama, "Stretchable liquid tactile sensor for robot-joints," in *2010 IEEE International Conference on Robotics and Automation*, 3-7 May 2010 2010, pp. 4212-4217, doi: 10.1109/ROBOT.2010.5509301.

[31] T. Helps and J. Rossiter, "Proprioceptive Flexible Fluidic Actuators Using Conductive Working Fluids," *Soft Robot*, vol. 5, no. 2, pp. 175-189, Apr 2018, doi: 10.1089/soro.2017.0012.

[32] H. A. Wurdemann *et al.*, "Embedded electro-conductive yarn for shape sensing of soft robotic manipulators," in *2015 37th Annual International Conference of the IEEE Engineering in Medicine and Biology Society (EMBC)*, 25-29 Aug. 2015 2015, pp. 8026-8029, doi: 10.1109/EMBC.2015.7320255.

[33] K. Kure, T. Kanda, K. Suzumori, and S. Wakimoto, "Flexible displacement sensor using injected conductive paste," *Sensors and Actuators A: Physical*, vol. 143, no. 2, pp. 272-278, 2008/05/16/ 2008, doi: https://doi.org/10.1016/j.sna.2007.11.031.

[34] S. Kuriyama, M. Ding, Y. Kurita, J. Ueda, Ogasawara, and Tsukasa, "Flexible Sensor for McKibben Pneumatic Artificial Muscle Actuator," *International Journal of Automation Technology*, vol. 3, no. 6, pp. 731-740, 2009, doi: 10.20965/ijat.2009.p0731.

[35] A. Koivikko, E. S. Raei, M. Mosallaei, M. Mäntysalo, and V. Sariola, "Screen-Printed Curvature Sensors for Soft Robots," *IEEE Sensors Journal*, vol. 18, no. 1, pp. 223-230, 2018, doi: 10.1109/JSEN.2017.2765745.

[36] P. M. Khin *et al.*, "Soft haptics using soft actuator and soft sensor," in *2016 6th IEEE International Conference on Biomedical Robotics and Biomechatronics (BioRob)*, 26-29 June 2016 2016, pp. 1272-1276, doi: 10.1109/BIOROB.2016.7523806.

[37] H. Zhang and M. Y. Wang, "Multi-Axis Soft Sensors Based on Dielectric Elastomer," *Soft Robotics*, vol. 3, no. 1, pp. 3-12, 2016, doi: 10.1089/soro.2015.0017.

[38] A. Sadeghi *et al.*, "A plant-inspired robot with soft differential bending capabilities," *Bioinspiration & Biomimetics*, vol. 12, no. 1, p. 015001, 2016/12/20 2016, doi: 10.1088/1748-3190/12/1/015001.

[39] S. Sareh, Y. Noh, M. Li, T. Ranzani, H. Liu, and K. Althoefer, "Macrobend optical sensing for pose measurement in soft robot arms," *Smart Materials and Structures*, vol. 24, no. 12, p. 125024, 2015/11/06 2015, doi: 10.1088/0964-1726/24/12/125024.

[40] S. Sareh *et al.*, "Bio-inspired tactile sensor sleeve for surgical soft manipulators," in *2014 IEEE International Conference on Robotics and Automation (ICRA)*, 31 May-7 June 2014 2014, pp. 1454-1459, doi: 10.1109/ICRA.2014.6907043.

[41] M. K. Dobrzynski, R. Pericet-Camara, and D. Floreano, "Contactless deflection sensor for soft robots," in *2011 IEEE/RSJ International Conference on Intelligent Robots and Systems*, 25-30 Sept. 2011 2011, pp. 1913-1918, doi: 10.1109/IROS.2011.6094845.

[42] J. C. Yeo, H. K. Yap, W. Xi, Z. Wang, C.-H. Yeow, and C. T. Lim, "Flexible and Stretchable Strain Sensing Actuator for Wearable Soft Robotic Applications," *Advanced Materials Technologies*, vol. 1, no. 3, p. 1600018, 2016, doi: 10.1002/admt.201600018.

[43] M. Amjadi, A. Pichitpajongkit, S. Lee, S. Ryu, and I. Park, "Highly Stretchable and Sensitive Strain Sensor Based on Silver Nanowire–Elastomer Nanocomposite," *ACS Nano*, vol. 8, no. 5, pp. 5154-5163, 2014/05/27 2014, doi: 10.1021/nn501204t.

[44] Y. Cheng, R. Wang, J. Sun, and L. Gao, "A Stretchable and Highly Sensitive Graphene-Based Fiber for Sensing Tensile Strain, Bending, and Torsion," *Advanced Materials*, vol. 27, no. 45, pp. 7365-7371, 2015, doi: 10.1002/adma.201503558.

[45] H. Wang, M. Totaro, and L. Beccai, "Toward Perceptive Soft Robots: Progress and Challenges," *Advanced Science*, vol. 5, no. 9, p. 1800541, 2018, doi: 10.1002/advs.201800541.

[46] A. Hirsch, "The era of carbon allotropes," *Nature Materials*, vol. 9, no. 11, pp. 868-871, 2010/11/01 2010, doi: 10.1038/nmat2885.

[47] H. W. Kroto, J. R. Heath, S. C. O'Brien, R. F. Curl, and R. E. Smalley, "C60: Buckminsterfullerene," *Nature*, vol. 318, no. 6042, pp. 162-163, 1985/11/01 1985, doi: 10.1038/318162a0.

[48] K. S. Novoselov *et al.*, "Electric Field Effect in Atomically Thin Carbon Films," *Science*, vol. 306, no. 5696, pp. 666-669, 2004, doi: 10.1126/science.1102896.

[49] P. M. Ajayan, "Nanotubes from Carbon," *Chemical Reviews*, vol. 99, no. 7, pp. 1787-1800, 1999/07/01 1999, doi: 10.1021/cr970102g.

[50] M. S. Dresselhaus, G. Dresselhaus, P. C. Eklund, and A. M. Rao, "Carbon Nanotubes," in *The Physics of Fullerene-Based and Fullerene-Related Materials*, W. Andreoni Ed. Dordrecht: Springer Netherlands, 2000, pp. 331-379.

[51] F. Varchon *et al.*, "Electronic Structure of Epitaxial Graphene Layers on SiC: Effect of the Substrate," *Physical Review Letters*, vol. 99, no. 12, p. 126805, 09/20/ 2007, doi: 10.1103/PhysRevLett.99.126805.

[52] R. S. Ruoff, D. Qian, and W. K. Liu, "Mechanical properties of carbon nanotubes: theoretical predictions and experimental measurements," *Comptes Rendus Physique*, vol. 4, no. 9, pp. 993-1008, 2003/11/01/ 2003, doi: https://doi.org/10.1016/j.crhy.2003.08.001.

[53] M.-F. Yu, B. S. Files, S. Arepalli, and R. S. Ruoff, "Tensile Loading of Ropes of Single Wall Carbon Nanotubes and their Mechanical Properties," *Physical Review Letters,* vol. 84, no. 24, pp. 5552-5555, 06/12/ 2000, doi: 10.1103/PhysRevLett.84.5552.

[54] M.-F. Yu, O. Lourie, M. J. Dyer, K. Moloni, T. F. Kelly, and R. S. Ruoff, "Strength and Breaking Mechanism of Multiwalled Carbon Nanotubes Under Tensile Load," *Science,* vol. 287, no. 5453, pp. 637-640, 2000, doi: 10.1126/science.287.5453.637.

[55] O. Lourie and H. D. Wagner, "Evaluation of Young's Modulus of Carbon Nanotubes by Micro-Raman Spectroscopy," *Journal of Materials Research,* vol. 13, no. 9, pp. 2418-2422, 1998, doi: 10.1557/JMR.1998.0336.

[56] T. W. Ebbesen, H. J. Lezec, H. Hiura, J. W. Bennett, H. F. Ghaemi, and T. Thio, "Electrical conductivity of individual carbon nanotubes," *Nature,* vol. 382, no. 6586, pp. 54-56, 1996/07/01 1996, doi: 10.1038/382054a0.

[57] E. A. Laird *et al.*, "Quantum transport in carbon nanotubes," *Reviews of Modern Physics,* vol. 87, no. 3, pp. 703-764, 07/28/ 2015, doi: 10.1103/RevModPhys.87.703.

[58] W. Obitayo and T. Liu, "A Review: Carbon Nanotube-Based Piezoresistive Strain Sensors," (in English), *Journal of Sensors,* 2012, doi: Artn 65243810.1155/2012/652438.

[59] R. Saito, G. Dresselhaus, and M. S. Dresselhaus, "Electronic structure of double-layer graphene tubules," *Journal of Applied Physics,* vol. 73, no. 2, pp. 494-500, 1993, doi: 10.1063/1.353358.

[60] T. W. Tombler *et al.*, "Reversible electromechanical characteristics of carbon nanotubes underlocal-probe manipulation," *Nature,* vol. 405, no. 6788, pp. 769-772, 2000/06/01 2000, doi: 10.1038/35015519.

[61] C. T. White and T. N. Todorov, "Carbon nanotubes as long ballistic conductors," *Nature,* vol. 393, no. 6682, pp. 240-242, 1998/05/01 1998, doi: 10.1038/30420.

[62] P. T. Araujo *et al.*, "In Situ Atomic Force Microscopy Tip-Induced Deformations and Raman Spectroscopy Characterization of Single-Wall Carbon Nanotubes," *Nano Letters,* vol. 12, no. 8, pp. 4110-4116, 2012/08/08 2012, doi: 10.1021/nl3016347.

[63] S. Paulson *et al.*, "In situ resistance measurements of strained carbon nanotubes," *Applied Physics Letters,* vol. 75, no. 19, pp. 2936-2938, 1999, doi: 10.1063/1.125193.

[64] R. Juarez-Mosqueda, M. Ghorbani-Asl, A. Kuc, and T. Heine, "Electromechanical Properties of Carbon Nanotubes," *The Journal of Physical Chemistry C,* vol. 118, no. 25, pp. 13936-13944, 2014/06/26 2014, doi: 10.1021/jp502267d.

[65] V. V. Ivanovskaya, N. Ranjan, T. Heine, G. Merino, and G. Seifert, "Molecular Dynamics Study of the Mechanical and Electronic Properties of Carbon Nanotubes," *Small*, vol. 1, no. 4, pp. 399-402, 2005, doi: 10.1002/smll.200400110.

[66] J. Sirohi and I. Chopra, "Fundamental Understanding of Piezoelectric Strain Sensors," *Journal of Intelligent Material Systems and Structures*, vol. 11, no. 4, pp. 246-257, 2000, doi: 10.1106/8bfb-gc8p-xq47-ycq0.

[67] V. Bhatia and A. M. Vengsarkar, "Optical fiber long-period grating sensors," *Opt. Lett.*, vol. 21, no. 9, pp. 692-694, 1996/05/01 1996, doi: 10.1364/OL.21.000692.

[68] H. J. Patrick, G. M. Williams, A. D. Kersey, J. R. Pedrazzani, and A. M. Vengsarkar, "Hybrid fiber Bragg grating/long period fiber grating sensor for strain/temperature discrimination," *IEEE Photonics Technology Letters*, vol. 8, no. 9, pp. 1223-1225, 1996, doi: 10.1109/68.531843.

[69] W. Qiu, Y. L. Kang, Z. K. Lei, Q. H. Qin, Q. Li, and Q. Wang, "Experimental study of the Raman strain rosette based on the carbon nanotube strain sensor," *Journal of Raman Spectroscopy*, vol. 41, no. 10, pp. 1216-1220, 2010.

[70] N. Anderson, N. Szorc, V. Gunasekaran, S. Joshi, and G. Jursich, "Highly sensitive screen printed strain sensors on flexible substrates via ink composition optimization," *Sensors and Actuators A: Physical*, vol. 290, pp. 1-7, 2019.

[71] B. Andò and S. Baglio, "All-Inkjet Printed Strain Sensors," *IEEE Sensors Journal*, vol. 13, no. 12, pp. 4874-4879, 2013, doi: 10.1109/JSEN.2013.2276271.

[72] S. Agarwala, G. L. Goh, and W. Y. Yeong, "Aerosol Jet Printed Strain Sensor: Simulation Studies Analyzing the Effect of Dimension and Design on Performance (September 2018)," *IEEE Access*, vol. 6, pp. 63080-63086, 2018, doi: 10.1109/ACCESS.2018.2876647.

[73] M. Al-Rubaiai, R. Tsuruta, U. Gandhi, C. Wang, and X. Tan, "A 3D-printed stretchable strain sensor for wind sensing," *Smart Materials and Structures*, vol. 28, no. 8, p. 084001, 2019/06/24 2019, doi: 10.1088/1361-665x/ab1fa9.

[74] H.-l. Yan *et al.*, "Coaxial printing method for directly writing stretchable cable as strain sensor," *Applied Physics Letters*, vol. 109, no. 8, p. 083502, 2016.

[75] C. Nothnagle, J. R. Baptist, J. Sanford, W. H. Lee, D. O. Popa, and M. B. Wijesundara, "EHD printing of PEDOT: PSS inks for fabricating pressure and strain sensor arrays on flexible substrates," in *Next-Generation Robotics II; and Machine Intelligence and Bio-inspired Computation: Theory and Applications IX*, 2015, vol. 9494: International Society for Optics and Photonics, p. 949403.

[76] T. Yamashita, H. Okada, T. Itoh, and T. Kobayashi, "Manufacturing process for piezoelectric strain sensor sheet involving transfer printing methods," *Japanese*

Journal of Applied Physics, vol. 54, no. 10S, p. 10ND08, 2015/09/17 2015, doi: 10.7567/jjap.54.10nd08.

[77] X. Lin, J. Kavalakkatt, M. C. Lux-Steiner, and A. Ennaoui, "Inkjet-Printed Cu2ZnSn (S, Se) 4 Solar Cells," *Advanced Science*, vol. 2, no. 6, p. 1500028, 2015.

[78] R. D. Nagel, T. Haeberle, M. Schmidt, P. Lugli, and G. Scarpa, "Large area nano-transfer printing of sub-50-nm metal nanostructures using low-cost semi-flexible hybrid templates," *Nanoscale research letters*, vol. 11, no. 1, p. 143, 2016.

[79] S. Luo and T. Liu, "Structure–property–processing relationships of single-wall carbon nanotube thin film piezoresistive sensors," *Carbon*, vol. 59, pp. 315-324, 2013.

[80] M. Hempel, D. Nezich, J. Kong, and M. Hofmann, "A novel class of strain gauges based on layered percolative films of 2D materials," *Nano letters*, vol. 12, no. 11, pp. 5714-5718, 2012.

[81] F. Bonaccorso, A. Bartolotta, J. N. Coleman, and C. Backes, "2D-crystal-based functional inks," *Advanced Materials*, vol. 28, no. 29, pp. 6136-6166, 2016.

[82] C. Yan *et al.*, "Highly stretchable piezoresistive graphene–nanocellulose nanopaper for strain sensors," *Advanced materials*, vol. 26, no. 13, pp. 2022-2027, 2014.

[83] D. J. Cohen, D. Mitra, K. Peterson, and M. M. Maharbiz, "A highly elastic, capacitive strain gauge based on percolating nanotube networks," *Nano letters*, vol. 12, no. 4, pp. 1821-1825, 2012.

[84] Y. Wang *et al.*, "Wearable and highly sensitive graphene strain sensors for human motion monitoring," *Advanced Functional Materials*, vol. 24, no. 29, pp. 4666-4670, 2014.

[85] L. Cai *et al.*, "Super-stretchable, transparent carbon nanotube-based capacitive strain sensors for human motion detection," *Scientific reports*, vol. 3, no. 1, pp. 1-9, 2013.

[86] N. Hu, Y. Karube, C. Yan, Z. Masuda, and H. Fukunaga, "Tunneling effect in a polymer/carbon nanotube nanocomposite strain sensor," *Acta Materialia*, vol. 56, no. 13, pp. 2929-2936, 2008.

[87] L. Lin *et al.*, "Towards tunable sensitivity of electrical property to strain for conductive polymer composites based on thermoplastic elastomer," *ACS applied materials & interfaces*, vol. 5, no. 12, pp. 5815-5824, 2013.

[88] L. Duan *et al.*, "The resistivity–strain behavior of conductive polymer composites: stability and sensitivity," *Journal of Materials Chemistry A*, vol. 2, no. 40, pp. 17085-17098, 2014.

[89] C. Lee, L. Jug, and E. Meng, "High strain biocompatible polydimethylsiloxane-based conductive graphene and multiwalled carbon nanotube nanocomposite strain sensors," *Applied Physics Letters,* vol. 102, no. 18, p. 183511, 2013.

[90] H. Gercek, "Poisson's ratio values for rocks," *International Journal of Rock Mechanics and Mining Sciences,* vol. 44, no. 1, pp. 1-13, 2007.

[91] M. Amjadi, K. U. Kyung, I. Park, and M. Sitti, "Stretchable, skin-mountable, and wearable strain sensors and their potential applications: a review," *Advanced Functional Materials,* vol. 26, no. 11, pp. 1678-1698, 2016.

[92] Alamusi *et al.*, "Ultrasensitive strain sensors of multiwalled carbon nanotube/epoxy nanocomposite using dielectric loss tangent," *Applied Physics Letters,* vol. 103, no. 22, p. 221903, 2013.

[93] Z. Jing, Z. Guang-Yu, and S. Dong-Xia, "Review of graphene-based strain sensors," *Chinese Physics B,* vol. 22, no. 5, p. 057701, 2013.

[94] G. Ambrosetti, C. Grimaldi, I. Balberg, T. Maeder, A. Danani, and P. Ryser, "Solution of the tunneling-percolation problem in the nanocomposite regime," *Physical Review B,* vol. 81, no. 15, p. 155434, 2010.

[95] J. C. Huang, "Carbon black filled conducting polymers and polymer blends," *Advances in Polymer Technology: Journal of the Polymer Processing Institute,* vol. 21, no. 4, pp. 299-313, 2002.

[96] P. Costa, A. Maceiras, M. San Sebastián, C. García-Astrain, J. Vilas, and S. Lanceros-Mendez, "On the use of surfactants for improving nanofiller dispersion and piezoresistive response in stretchable polymer composites," *Journal of Materials Chemistry C,* vol. 6, no. 39, pp. 10580-10588, 2018.

[97] Y. Zheng *et al.*, "A highly stretchable and stable strain sensor based on hybrid carbon nanofillers/polydimethylsiloxane conductive composites for large human motions monitoring," *Composites Science and Technology,* vol. 156, pp. 276-286, 2018.

[98] J. Y. Oh, G. H. Jun, S. Jin, H. J. Ryu, and S. H. Hong, "Enhanced electrical networks of stretchable conductors with small fraction of carbon nanotube/graphene hybrid fillers," *ACS applied materials & interfaces,* vol. 8, no. 5, pp. 3319-3325, 2016.

[99] S. Wang *et al.*, "Network cracks-based wearable strain sensors for subtle and large strain detection of human motions," *Journal of Materials Chemistry C,* vol. 6, no. 19, pp. 5140-5147, 2018.

[100] J. G. Simmons, "Electric tunnel effect between dissimilar electrodes separated by a thin insulating film," *Journal of applied physics,* vol. 34, no. 9, pp. 2581-2590, 1963.

[101] L. Lin *et al.*, "Modified resistivity–strain behavior through the incorporation of metallic particles in conductive polymer composite fibers containing carbon nanotubes," *Polymer international,* vol. 62, no. 1, pp. 134-140, 2013.

[102] N. Lu, C. Lu, S. Yang, and J. Rogers, "Highly sensitive skin-mountable strain gauges based entirely on elastomers," *Advanced Functional Materials,* vol. 22, no. 19, pp. 4044-4050, 2012.

[103] C. Pang, C. Lee, and K. Y. Suh, "Recent advances in flexible sensors for wearable and implantable devices," *Journal of Applied Polymer Science,* vol. 130, no. 3, pp. 1429-1441, 2013.

[104] X. Xiao *et al.*, "High-strain sensors based on ZnO nanowire/polystyrene hybridized flexible films," *Advanced materials,* vol. 23, no. 45, pp. 5440-5444, 2011.

[105] T. Yamada *et al.*, "A stretchable carbon nanotube strain sensor for human-motion detection," *Nature nanotechnology,* vol. 6, no. 5, p. 296, 2011.

[106] M. Amjadi, Y. J. Yoon, and I. Park, "Ultra-stretchable and skin-mountable strain sensors using carbon nanotubes–Ecoflex nanocomposites," *Nanotechnology,* vol. 26, no. 37, p. 375501, 2015.

[107] Q. Zhang *et al.*, "Highly sensitive and stretchable strain sensor based on Ag@ CNTs," *Nanomaterials,* vol. 7, no. 12, p. 424, 2017.

[108] I. Kang, M. J. Schulz, J. H. Kim, V. Shanov, and D. Shi, "A carbon nanotube strain sensor for structural health monitoring," *Smart materials and structures,* vol. 15, no. 3, p. 737, 2006.

[109] A. P. Gerratt, H. O. Michaud, and S. P. Lacour, "Elastomeric electronic skin for prosthetic tactile sensation," *Advanced Functional Materials,* vol. 25, no. 15, pp. 2287-2295, 2015.

[110] S. Gong *et al.*, "Highly Stretchy Black Gold E-Skin Nanopatches as Highly Sensitive Wearable Biomedical Sensors," *Advanced Electronic Materials,* vol. 1, no. 4, p. 1400063, 2015.

[111] M. A. McEvoy and N. Correll, "Materials that couple sensing, actuation, computation, and communication," *Science,* vol. 347, no. 6228, p. 1261689, 2015, doi: 10.1126/science.1261689.

[112] C. Majidi, "Soft Robotics: A Perspective—Current Trends and Prospects for the Future," *Soft Robotics,* vol. 1, no. 1, pp. 5-11, 2014, doi: 10.1089/soro.2013.0001.

[113] J. A. Fan *et al.*, "Fractal design concepts for stretchable electronics," *Nature Communications,* vol. 5, no. 1, p. 3266, 2014/02/07 2014, doi: 10.1038/ncomms4266.

[114] T. Widlund, S. Yang, Y.-Y. Hsu, and N. Lu, "Stretchability and compliance of freestanding serpentine-shaped ribbons," *International Journal of Solids and Structures,* vol. 51, no. 23, pp. 4026-4037, 2014/11/01/ 2014, doi: https://doi.org/10.1016/j.ijsolstr.2014.07.025.

[115] Q. Ma and Y. Zhang, "Mechanics of Fractal-Inspired Horseshoe Microstructures for Applications in Stretchable Electronics," *Journal of Applied Mechanics,* vol. 83, no. 11, 2016, doi: 10.1115/1.4034458.

[116] D.-H. Kim *et al.*, "Epidermal Electronics," *Science,* vol. 333, no. 6044, pp. 838-843, 2011, doi: 10.1126/science.1206157.

[117] W.-H. Yeo *et al.*, "Multifunctional Epidermal Electronics Printed Directly Onto the Skin," *Advanced Materials,* vol. 25, no. 20, pp. 2773-2778, 2013, doi: 10.1002/adma.201204426.